Long-Term Monthly 0.05° Terrestrial Evapotranspiration Dataset (1982-2018) for the Tibetan Plateau

Ling Yuan [1,2], Xuelong Chen[1,4,6]*, Yaoming Ma[1,2,3,4,5,6]*, Cunbo Han[1,4,6], Binbin Wang[1,4,5,6], Weiqiang Ma[1,4,6]

[1] Land-Atmosphere Interaction and its Climatic Effects Group, State Key Laboratory of Tibetan Plateau Earth System, Environment and Resources (TPESRE), Institute of Tibetan Plateau Research, Chinese Academy of Sciences, Beijing 100101, China.

[2] College of Earth and Planetary Sciences, University of Chinese Academy of Sciences, Beijing 100049, China

[3] College of Atmospheric Science, Lanzhou University, Lanzhou 730000, China

[4] National Observation and Research Station for Qomolongma Special Atmospheric Processes and Environmental Changes, Dingri 858200, China

[5] Kathmandu Center of Research and Education, Chinese Academy of Sciences, Beijing 100101, China

[6] China-Pakistan Joint Research Center on Earth Sciences, Chinese Academy of Sciences, Islamabad 45320, Pakistan

Corresponding author and address:

Xuelong Chen, Dr., Prof., x.chen@itpcas.ac.cn

Yaoming Ma, Dr., Prof., ymma@itpcas.ac.cn

Building 3, No.16 Lincui Road, Chaoyang District, Beijing 100101, China

Abstract

Evapotranspiration (*ET*) plays a crucial role in the water balance of the Tibetan Plateau (TP), often referred to as the "Asian water tower" region. However, accurately monitoring and comprehending the spatial and temporal variations of ET components (including soil evaporation E_s, canopy transpiration E_c, and intercepted water evaporation E_w) in this remote area remains a significant challenge due to the limited availability of observational data. In this study, a 37-year dataset (1982–2018) of monthly *ET* components for the TP using the MOD16-STM (MOD16 soil texture model) are generated. This model utilizes up-to-date soil properties, meteorological data, and remote sensing datasets. The estimated *ET* results exhibit a strong correlation with measurements from nine flux towers, demonstrating a low root mean square error of 13.48 mm/month, a mean bias of 2.85 mm/month, a coefficient of determination of 0.83, and an index of agreement of 0.92. The annual averaged *ET* for the entire TP, defined as elevations higher than 2500 m, is approximately 0.93±0.037 Gt/year. The predominant contributor to *ET* on the TP is E_s, accounting for 84% of the total *ET*. Our findings reveal a noteworthy upward trend in ET in most central and eastern parts of the TP, with a rate of approximately 1–4 mm/year (p<0.05) and a significant downward trend with a rate of −3–1 mm/year in the northwestern part of TP during the period from 1982 to 2018. The average annual increase in *ET* for the entire TP over the past 37 years is approximately 0.96 mm/year. This upward trend can be attributed to the warming and wetting climate conditions on the TP. The MOD16-STM *ET* dataset demonstrates a reliable performance across the TP when compared to previous research outcomes. This dataset serves as a valuable resource for research in water resource management, drought monitoring, and ecological studies. The entire dataset is freely accessible through the Science Data Bank (http://doi.org/10.11922/sciencedb.00020, Y. Ma*, X. Chen*, L. Yuan, 2021) and the National Tibetan Plateau Data Center (TPDC) (https://data.tpdc.ac.cn/en/disallow/e253621a-6334-4ad1-b2b9-e1ce2aa9688f/, http://doi.org/10.11888/Terre.tpdc.271913, L. Yuan, X. Chen*, Y. Ma*, 2021).

Keywords: Evapotranspiration; MOD16-STM; Climate change; Asian water tower; Tibetan Plateau

1. Introduction

The Tibetan Plateau (TP) (24–40°N, 70–105°E) is often referred to as the "Asian water tower" owing to its distinctive geographical and ecological characteristics, as acknowledged in studies by Immerzeel et al. (2010, 2020) and Yao et al. (2012). Within this region, evapotranspiration (*ET*) plays a vital role in the overall water balance. The TP predominantly features grassland (covering more than 47% of the area) and sparse vegetation or bare soil (covering over 33%), as indicated by the Moderate Resolution Imaging Spectroradiometer (MODIS) land cover dataset (MCD12C1) (Fig. 1c). This vast expanse is mostly characterized by arid or semi-arid conditions. The TP is currently undergoing significant changes in its hydrological cycle, driven by global warming, as documented in studies by Yang et al. (2014), Kuang et al. (2016), and Zohaib et al. (2017). Nevertheless, accurately monitoring the spatial and temporal fluctuations in ET on the TP remains a formidable challenge due to the intricate environmental conditions of the TP. Moreover, understanding how *ET* patterns on the TP will evolve in the context of global warming is essential for assessing the impacts of these changes on the local population's livelihoods.

In recent years, various datasets for estimating *ET* on the TP have been developed, including the complementary relationship (CR) model (Ma et al., 2019; Wang et al., 2020), the surface energy balance system (SEBS) model (Chen et al., 2014, 2021; Zhong et al., 2019; Han et al., 2017, 2021), and the Penman–Monteith model with remote sensing (RS-PM) (Wang et al., 2018; Song et al., 2017; Chang et al., 2018; Ma et al., 2022), among others. However, there still exists a considerable variance among these *ET* products for the TP (Peng et al., 2016; Baik et al., 2018; Li et al., 2018; Khan et al., 2018). Studies have utilized eddy-covariance measurements (Shi et al., 2014; You et al., 2017; Yang et al., 2019; Ma et al., 2020) and reanalysis datasets (Shi et al., 2014; Dan et al., 2017; Yang et al., 2019; De Kok et al., 2020) to investigate *ET* on the TP. A recent study by Han et al. (2021) produced an 18-year ET dataset (2001–2018) for the region. Enhancements to the canopy conduction algorithm in the Penman–Monteith model have led to improved *ET* estimates in previous research (Leuning et al., 2008; Zhang et al., 2010; Li et al., 2015; Zhang et al., 2016, 2019a; Gan et al., 2018). However, these *ET* products tend to perform poorly in TP areas with sparse vegetation, arid to semi-arid climates (Zhang et al., 2010; Li et al., 2014b; Song et al., 2017; Baik et al., 2018; Li et al., 2018; Khan et al., 2018).

The limitations of the MOD16 Penman–Monteith model in arid to semi-arid TP regions are primarily due to its failure to consider the dominant role of topsoil texture and topsoil moisture in governing E_s processes (Yuan et al., 2021). Accurately separating and validating *ET* components on the TP remains challenging, even

though total *ET* estimates tend to align across different products (Lawrence et al., 2007; Blyth and Harding, 2011; Miralles et al., 2016). The TP is primarily characterized by short and sparse vegetation, and soil moisture plays a crucial role in *ET* estimation for this region. Several studies have used the Penman–Monteith algorithm to estimate *ET* on the TP (Wang et al., 2018; Ma et al., 2022). However, these studies have not accounted for the effects of soil moisture (*SM*) on evaporation resistance and stomatal conductance.

To address these limitations, the enhanced Penman–Monteith model, known as MOD16-STM (MOD16 soil texture model), has been developed. MOD16-STM redefines the modules for E_s to consider the impacts of *SM* on soil evaporation resistance. This modification is based on eddy-covariance (*EC*) observations conducted on the TP (Yuan et al., 2021), offering a promising opportunity to accurately estimate *ET* components in this region. E_s often dominates *ET* in sparsely vegetated areas, especially in arid and semi-arid regions with large bare soil areas (Wilcox et al., 2003; Kool et al., 2014; Wang et al., 2018; Ma et al., 2015a, 2015b; Ma and Zhang, 2022). Previous studies have highlighted that 20% to 40% of global *ET* is attributed to E_s. Bare soil surface evaporation is a rapid process influenced by shallow surface water (Koster and Suarez, 1996). E_s is primarily controlled by water diffusion in the soil (Good et al., 2015; Yuan et al., 2021). Accurately quantifying, and separating E_s is crucial for enhancing our understanding of water and energy cycles on the TP. However, quantifying *ET* and its components remains challenging due to the influence of atmospheric demand, soil moisture conditions, and complex interactions between heterogeneous vegetation and soil properties (Merlin et al., 2016; Wu et al., 2017; Phillips et al., 2017; Lehmann et al., 2018). MOD16-STM holds the potential to generate a remote sensing E_s and *ET* component dataset covering the satellite era since 1980. In this study, the MOD16-STM model, acknowledging its limitations, was employed to estimate a long-term *ET* and *ET* components dataset spanning 37 years (1982–2018) (Yuan et al., 2021).

A preferable approach involves directly estimating *ET* based on topsoil moisture, which has a greater impact on surface water exchange on the TP. Thus, leveraging the advantages of the MOD16-STM model for *ET* estimation on the TP, this study aimed to achieve two main objectives: (1) develop a 37-year (1982–2018) monthly *ET* dataset for the TP at a 0.05° × 0.05° spatial resolution; and (2) quantify the spatial distribution and spatiotemporal variability of *ET* and its components across the TP.

2. Materials and methods

2.1 Study area

The Tibetan Plateau, located between 25–40°N and 74–104°E, spans approximately 2.5 million km^2 and

consists of land above 2,500 m in altitude (Fig. 1a). This region, as indicated by the FAO drought index dataset, represents the largest landform unit in Eurasia and encompasses hyper-arid, arid, semi-arid, and sub-humid climate zones (Fig. 1b). The land cover types primarily include mixed forests, grasslands, bare soil, glaciers, and snow-covered areas (see Fig. 1c). The topsoil predominantly consists of sandy loam, loam, and clay (Fig. 1d). The annual average temperature in the region ranges from approximately −3.1°C to 4.4°C. Average annual precipitation gradually increases from less than 50 mm in the northwest to over 1000 mm in the southeast, with most of the precipitation occurring during the summer months (Ding et al., 2017). Over time, the TP has undergone significant environmental changes, including increased precipitation, decreased wind speed (*wind*), fewer snow days, reduced radiation, thawing permafrost, glacier melting, and increased vegetation (Yao et al., 2012; Yang et al., 2014; Kuang et al., 2016; Bibi et al., 2018; Chen et al., 2019).

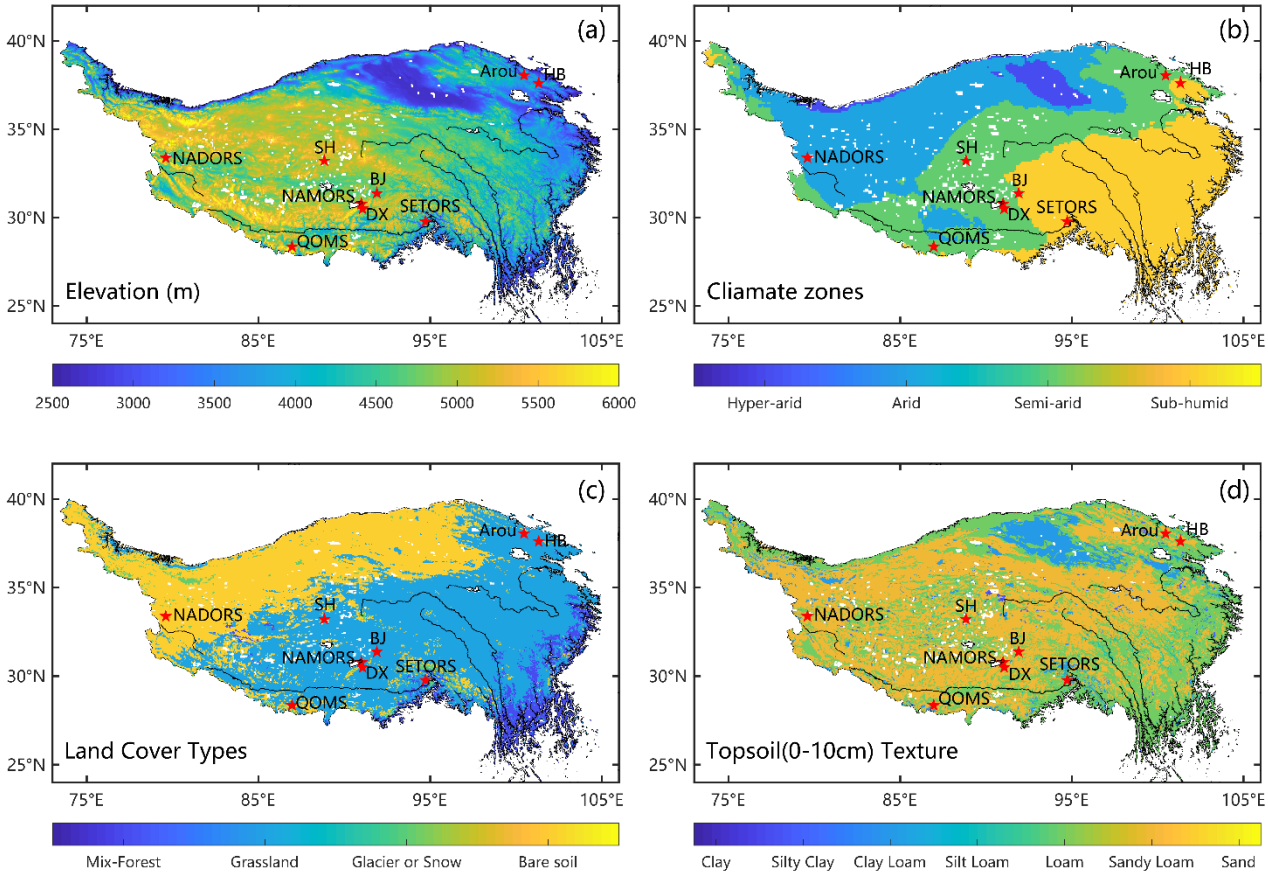

Figure 1. Maps of the (a) topography (STRM), (b) climate zones (FAO aridity index), (c) land cover types (MCD12C1), and (d) soil textures (HWSD) in the study area. The red dots indicate the flux site locations.

2.2 Generation of a long-term series of monthly *ET* products

This study introduces a novel dataset comprising a long-term series of monthly *ET*, which is generated

using the MOD16-STM model. The process of calculating monthly *ET* with the MOD16-STM model and the associated driving datasets is illustrated in Figure 2.

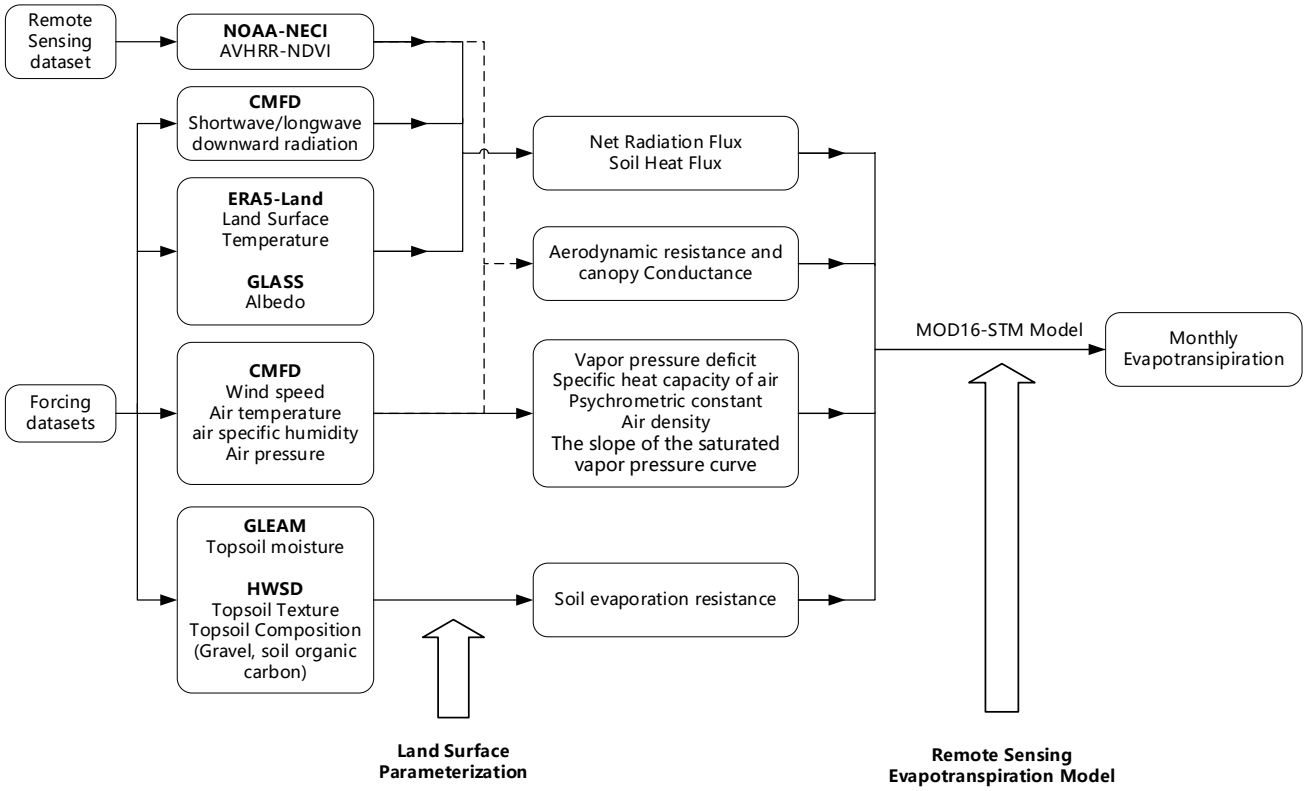

Figure 2. Workflow of the MOD16-STM evapotranspiration product.

2.2.1 Description of MOD16-STM *ET* model

The MOD16-STM model computes the ET components using the Penman–Monteith equation, as follows:

$$E_c = \frac{(\Delta \times f_c \times (R_n - G_0) + \rho_a \times C_p \times \frac{VPD}{r_a} \times f_c) \times (1 - F_{wet})}{\lambda \times \left(\Delta + \gamma \times (1 + \frac{r_c}{r_a})\right)} \quad (1)$$

$$E_s = \frac{(\Delta \times (1 - f_c) \times (R_n - G_0) + \rho_a \times C_p \times \frac{VPD}{r_a}) \times (1 - F_{wet})}{\lambda \times \left(\Delta + \gamma \times (1 + \frac{r_s}{r_a})\right)} \times \left(\frac{RH}{100}\right)^{\frac{VPD}{\beta}} \quad (2)$$

$$E_w = E_{wet\_s} + E_{wet\_c} \quad (3)$$

The total *ET* is the combined sum of three distinct components: E_c, E_s, and E_w (wet surface evaporation). For a more detailed explanation of the calculations for E_{wet_s} (evaporation from wet soil) and E_{wet_c} (evaporation from wet canopy), you can refer to Yuan et al. 2021. The variables used in above equations are defined as follows:

- R_n represents the net radiation flux ($W \cdot m^{-2}$).

- G_0 denotes the soil heat flux ($W \cdot m^{-2}$).
- ρ_a is the density of the air ($kg \cdot m^{-3}$).
- C_p stands for the specific heat capacity of the air ($J \cdot kg^{-1} \cdot K^{-1}$).
- VPD represents the vapor pressure deficit (hPa).
- Δ represents the slope of the saturated vapor pressure curve ($hPa \cdot K^{-1}$).
- γ is the psychrometric constant ($hPa \cdot K^{-1}$), calculated as $\gamma = C_p \cdot P_a \cdot M_a/(\lambda \cdot M_w)$, where λ is the latent heat of vaporization ($J \cdot kg^{-1}$), and M_a and M_w are the molecular masses of dry air and wet air, respectively.
- r_a signifies the aerodynamic resistance ($s \cdot m^{-1}$).
- r_s represents the surface (or canopy) resistance ($s \cdot m^{-1}$).
- F_{wet} is the relative surface wetness.
- The vegetation cover fraction (fc) is estimated using the $NDVI$ (Normalized Difference Vegetation Index).

$$f_c = \left(\frac{NDVI - NDVI_{\min}}{NDVI_{\max} + NDVI_{\min}} \right)^2 \tag{4}$$

R_n and G_0 are calculated as follows:

$$R_n = (1-\alpha) \times SWD + LWD - \varepsilon \times \sigma \times LST^4 \tag{5}$$

$$G_0 = R_n \times (I_c + (1-f_c) \times (I_s - I_c)) \tag{6}$$

here, SWD is the downward shortwave radiation, α is land surface albedo, LWD is the downward longwave radiation, σ represents the Stefan-Boltzmann constant ($5.67 \times 10^{-8}\ W \cdot m^{-2} \cdot K^{-4}$), ε is emissivity, and LST means land surface temperature. I_c (= 0.05) and I_s (= 0.315) are the ratios of ground heat flux and net radiation for surfaces with full vegetation cover (Su et al., 2002) and bare soil (determined by $NDVI < 0.25$ in this study) (Yuan et al., 2021), respectively. When the air temperature (T_a) is below 5°C, photosynthesis and transpiration processes are not active, and therefore, E_c is not considered in the calculations. Additionally, when the land surface temperature is below 0°C, the sublimation equation is derived by modifying the surface energy balance equation using the Clausius–Clapeyron equation, accounting for the equilibrium of water vapor in both liquid and frozen states. It's important to note that the evaporation from water surfaces was not estimated in this study. Previous research has extensively examined water surface evaporation from lakes on the TP in detail (Wang et al., 2020). Therefore, this study focuses on land ET estimation, excluding water surface evaporation.

Numerous prior studies have employed optimized conductance to estimate E_c (Jarvis et al., 1976; Irmak

and Mutiibwa, 2010; Zhang et al., 2010; Leuning et al., 2008; Li et al., 2013, 2015), as well as E_s (Sun et al., 1982; Camillo and Gurney, 1986; Sellers et al., 1996; Sakaguchi and Zeng, 2009; Ortega-Farias et al., 2010; Tang et al., 2013). In this study, the r_a was computed using the Monin-Obukhov similarity theory (MOST) (Liu et al., 2007).

$$r_a = \frac{ln\left(\frac{z_h - d_0}{z_{0h}} - \psi_h\right) ln\left(\frac{z_m - d_0}{z_{0m}} - \psi_m\right)}{k^2 u} \quad (7)$$

where k represents the von Karman's constant (0.41), z_h and z_m denote the measurement heights for T_a and *wind*, and d_0 represents the displacement height. The stability correction functions for momentum (ψ_m) and heat transfer (ψ_h) can be computed using universal functions. The mathematical expressions for these correction terms are as following.

For stable conditions:

$$\psi_m = -5.3\frac{(z_m - z_{0m})}{L} \quad (8)$$

$$\psi_h = -8.0\frac{z_h - z_{0h}}{L} \quad (9)$$

For unstable conditions:

$$\psi_m = 2\ln\left(\frac{1+x}{1+x_o}\right) + \ln\left(\frac{1+x^2}{1+x_o^2}\right) - 2\tan^{-1}x + 2\tan^{-1}x_o \quad (10)$$

$$\psi_h = 2\ln\left(\frac{1+y}{1+y_o}\right) \quad (11)$$

For neutral conditions:

$$\psi_m = \psi_h = 0 \quad (12)$$

In Equations (8–11), the following variables and parameters are defined:

- $x = (1 - z_m/L)^{0.25}$
- $x_o = (1 - z_{om}/L)^{0.25}$
- $y = (1 - 11.6\, z_h/\mathrm{L})^{0.5}$
- $y_o = (1 - 11.6\, z_{oh}/L)^{0.5}$

here, L represents the Obukhov length (m), calculated as $L = T_a \cdot u^{*2}/(k \cdot g \cdot T^*)$, where g = 9.8 m/s² and T^* is the fractional temperature (K). T^* is further defined as $T^* = -(\theta_s - \theta_a)/((\ln(z_h/z_{oh}) - \psi_h)$, where θ_s can be approximated using the *LST,* and $\theta_a = \mathrm{T_a} + z_h \cdot g/C_p$. The parameterization of u^* and L has been successfully applied in previous studies on the Tibetan Plateau (TP) (Chen et al., 2013). z_{0h} represents the roughness length for heat transfer (m).

A parameterization scheme for z_{0h} developed by Yang et al. (2008) has been widely utilized in remote sensing land surface fluxes and land surface models (LSMs) across the TP (Biermann et al., 2014; Chen et al., 2013; Ma et al., 2015b). This scheme has also been employed in the current study for consistency.

$$z_{0h} = \frac{70v}{u_*} exp(-7.2u_*^{0.5}|T^*|^{0.25}) \tag{13}$$

where v is the fluid kinematic viscosity, v=1.328×10^{-5}·(P_0·P_a^{-1})·(T_a·T_0^{-1})$^{1.754}$, P_0 = 1013 hPa and T_0 = 273.15 K. The roughness height for momentum transfer (z_{0m}) was determined based on canopy height (h_c), following the method outlined by Chen et al. (2013). The water saturation degree of surface soil (SM/θ_{sat}) is utilized to impose soil classification and soil texture constraints on the r_s and E_s estimates, as follows:

$$r_s = \exp\left(a + b \times \frac{SM}{\theta_{sat}}\right) \tag{14}$$

here, the parameters a and b are empirical coefficients that vary based on different soil textures, as documented in Table 1. The estimation of θ_{sat}, which considers soil organic content (SOC) and gravel content, can be obtained using the Soc-Vg scheme (Chen et al., 2012; Zhao et al., 2018).

$$\theta_{sat} = (1 - V_{SOC} - V_g) \times \theta_{sat,m} + V_{SOC} \times \theta_{sat,sc} \tag{15}$$

where $\theta_{sat,m}$ represents the porosity of the mineral soil and can be calculated as $\theta_{sat,m}$ = 0.489–0.00126·%sand (Cosby et al., 1984). Additionally, $\theta_{sat,sc}$ is the porosity of the SOC and is assumed to be 0.9 m^3·m^{-3} in this study, as per the work of Farouki (1981) and Letts et al. (2000). The variables V_{soc} and V_g denote the volumetric fractions of the SOC and gravel, respectively, and their calculation is as follows:

$$V_{SOC} = \frac{\rho_p \times (1 - \theta_{sat,m}) \times m_{SOC}}{\rho_{SOC} \times (1 - m_{SOC}) + \rho_p \times (1 - \theta_{sat,m}) \times m_{SOC} + (1 - \theta_{sat,m}) \times \frac{\rho_{SOC} \times m_g}{1 - m_g}} \tag{16}$$

$$V_g = \frac{\rho_{SOC} \times (1 - \theta_{sat,m}) \times m_g}{(1 - m_g) \times \left(\rho_{SOC} \times (1 - m_{SOC}) + \rho_p \times (1 - \theta_{sat,m}) \times m_{SOC} + (1 - \theta_{sat,m}) \times \frac{\rho_{SOC} \times m_g}{1 - m_g}\right)} \tag{17}$$

In these equations, ρ_p represents the mineral particle density and is set at 2700 kg/m^3, while ρ_{soc} is the bulk density of organic matter, maintained at 130 kg/m^3. Additionally, m_{soc} and m_g denote the percentages of organic matter and gravel, respectively, within topsoil layer.

The performance of soil surface resistance estimated by the MOD16-STM model at the site scale was demonstrated in Fig.3. The observations at the ten stations show that the soil surface resistance exponentially decrease with the increasing of SM/θ_{sat}. The MOD16-STM has caught this exponential law. It has a coefficient of determination (R^2) higher than 0.34, which may enable the model to reasonably estimate the TP ET.

Table 1. parameters *a* and *b* values based on different soil textures, which were used to calculate surface soil resistances.

Texture	$r_s = \exp\left(a + b \times \frac{SM}{\theta_{sat}}\right)$	
	a	***b***
Sandy Loam	7.65	-7.3
Sand	5.89	-8.17
Loamy Sand	8.02	-17.37
Silt Loam	7.09	-3.79
Loam	6.82	-4.33
Clay Loam	10.17	-7.43
Sandy Clay Loam	9.46	-4.52
Clay	10.02	-6.68
Silty Clay	11.67	-7.25
Silty Clay Loam	8.93	-9.14

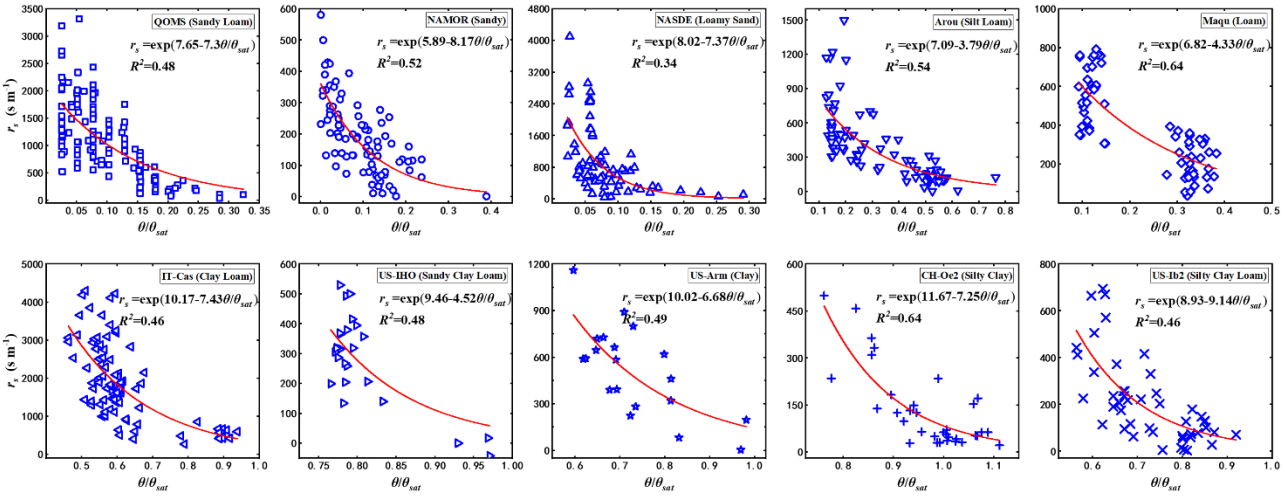

Figure 3. The scatter point relationship between soil surface resistance (r_s) and SM/θ_{sat} observed at QOMS (sandy loam), NAMOR (sandy), NASDE (loamy sand), Arou (silt loam), Maqu (loam), IT-CAS (clay loam), US-IHO (sandy clay loam), US-Arm (clay), CH-Oe2 (silty clay), and US-Ib2 (silty clay loam). The red curves show the equations used by MOD16-STM model. The site information is given in table 3 and A1.

2.2.2 Input data for calculating the TP *ET*

The MOD16-STM model relies on a range of remote sensing datasets, reanalysis datasets, and meteorological forcing datasets to estimate monthly *ET* across the TP. Specific datasets are carefully selected to minimize spatial and temporal gaps in the final product (Table 2). Here's a breakdown of the key datasets and

their sources:

- Monthly meteorological forcing data, including *wind*, T_a, air specific humidity (q), P_a, shortwave downward shortwave radiation, and downward longwave radiation, were obtained from the China Meteorological Forcing Dataset (CMFD) with a 0.1° spatial resolution for the period 1982–2018. This data source was accessed from the National Tibetan Plateau Data Center (Yang et al., 2010; He et al., 2020). CMFD can be downloaded from TPDC (https://data.tpdc.ac.cn/).
- *LST* and precipitation data were sourced from ERA5-Land, which provides data with a spatial resolution of 0.1° and a monthly temporal resolution. These datasets were obtained from the European Centre for Medium-Range Weather Forecasts (ECWMF).
- Albedo (α) data, with a spatial resolution of 0.05° and an 8-day temporal resolution, were derived from the Global Land Surface Satellite (GLASS) dataset (Liang et al., 2021).
- A long-term normalized difference vegetation index (NDVI) dataset, with a spatial resolution of 0.05° and daily temporal resolution, was acquired from the National Oceanic and Atmospheric Administration's National Centers for Environmental Information (NOAA-NCEI) (https://www.ncei.noaa.gov/products/climate-data-records/normalized-difference-vegetation-index). This dataset was used to calculate canopy height and Leaf Area Index (LAI) (Chen et al., 2013).
- A topsoil moisture dataset for the 0–10 cm depth, with a spatial resolution of 0.25° and a monthly temporal resolution, was obtained from the Global Land Evaporation Amsterdam Model (GLEAM) (Miralles et al., 2011).
- Upward longwave radiation (*LWU*) was derived from *LST* using the Stefan-Boltzmann Law. The emissivity of mixed pixels was calculated based on the specific emissivity values for vegetated and bare land surfaces, following Sobrino et al. (2004).
- Soil texture and soil property data were obtained from the Harmonized World Soil Database v1.2 (HWSD) (Wieder et al., 2014). These data were used to calculate soil evaporation resistance.

To ensure consistency, daily and 8-day input data were averaged over the temporal scale to create monthly datasets. If the ratio of valid data in any given month was below 90%, the averaged value was considered invalid. Additionally, the spatial resolutions of all input datasets were interpolated to a common 0.05° spatial resolution using a widely used bilinear interpolation method.

Table 2. Input datasets used to calculate the *ET* on the Tibetan Plateau.

	Data source	Temporal resolution	Availability	Domain	Spatial resolution	Method
SWD	CMFD	3 h	1979–2018	China land	0.1° × 0.1°	Reanalysis
LWD	CMFD	3 h	1979–2018	China land	0.1° × 0.1°	Reanalysis
T_a	CMFD	3 h	1979–2018	China land	0.1° × 0.1°	Reanalysis
q	CMFD	3 h	1979–2018	China land	0.1° × 0.1°	Reanalysis
wind	CMFD	3 h	1979–2018	China land	0.1° × 0.1°	Reanalysis
P_a	CMFD	3 h	1979–2018	China land	0.1° × 0.1°	Reanalysis
Precipitation	CMFD	3 h	1979–2018	China land	0.1° × 0.1°	Reanalysis
LST	ERA5	Monthly	1981–2021	Global	0.1° × 0.1°	Reanalysis
α	GLASS	8 days	1981–2019	Global	0.05° × 0.05°	Satellite
NDVI	AVHRR	Daily	1981–2019	Global	0.05° × 0.05°	Satellite
SM	GLEAM	Monthly	1979–2019	Global	0.25° x 0.25°	Reanalysis
Soil Properties	HWSD	/	/	China land	0.083°/1 km	/

2.3 Validation methods

2.3.1 Model validation at site scale

There are limited stations on the TP, which makes it impossible to collect ET observation at all kinds of soil texture. Hereby, we have collected datasets from 17 flux sites which are locating outside of the TP (Table A1 in Appendix A). Five sites are used to verify the relationship between soil surface resistance and SM/θ_{sat}. This result was presented in Fig. 3. The rest twelve verification sites include ten different soil textures (sandy loam, sand, loamy sand, silt loam, loam, clay loam, sandy clay loam, clay, silty clay, and silty clay loam) and three surface cover types (grassland, evergreen forest, and cropland) (Table A1). These twelve sites were used to do model validation at site scale. When evaluating the MOD16-STM at site scale, the meteorological forcing data comes from the station measurement. This helps us to minimize the simulation uncertainty due to the errors in the model forcing datasets. This methodology can help us to diagnosis the model`s limitation for representing the evapotranspiration process. Fig. A1 shows that MOD16-STM can capture the *ET* variations at the twelve sites. Table A2 also list the statistical values of the daily *ET* estimation. Since these sites include all kinds of soil texture and different canopy covers, it makes us believe that MOD16-STM model could be applied to the TP regional scale.

2.3.2 *ET* product evaluation

The remote sensing *ET* product was validated through comparison with flux tower observations on the TP. Table 3 list details of nine flux stations on the Tibetan Plateau, used for the ET product evaluation. These stations belongs to the China-Flux (Dang-Xiong site (DX), Hai-Bei site (HB), Yu et al., 2006; Zhang et al., 2019a), the Tibetan Observation and Research Platform (TORP) (BJ, NADORS, SETORS, QOMS, NAMORS, and Shuang-Hu (SH), Ma et al., 2020), and the Heihe Watershed Allied Telemetry Experimental Research (HiWATER) (Arou, Liu et al., 2011, 2018; Che et al., 2019) networks. The nine stations were in areas with three different land cover types: alpine meadow, alpine steppe, and Gobi. Half-hourly flux data measured by eddy-covariance from the nine stations were collected. It's important to note that the energy balance closure ratio (ECR) indicates whether the sum of sensible heat (H), latent heat (LE), and soil heat flux (G_0) matches the R_n. To ensure the reliability of eddy-covariance measurements, half-hourly data were screened and corrected accordingly. Half-hourly LE data was corrected using the bowen ratio energy balance correction method (Chen et al., 2014).

$$ECR = \frac{H + LE}{R_n - G_0} \tag{18}$$

$$LE_{cor} = \frac{1}{ECR} \times LE \tag{19}$$

Table 3. Details of the nine flux observation stations on the Tibetan Plateau, used for the *ET* product evaluation

Sites	Long., Lat.	Land cover type	Elevation (m)	Availability	Climate zone	Reference
Shuang-Hu (SH)	88.83°E, 33.21°N	Alpine meadow	4947	2013–2018	Semi-arid	
BJ	91.90°E, 31.37°N	Alpine meadow	4509	2010–2016	Semi-arid	
NADORS	79.60°E, 33.38°N	Alpine steppe	4264	2010–2018	Arid	Ma et al., 2020
SETORS	94.73°E, 29.77°N	Alpine meadow	3326	2007–2018	Sub-humid	
QOMS	86.95°E, 28.35°N	Gobi	4276	2007–2018	Semi-arid	
NAMORS	90.99°E, 30.77°N	Alpine meadow	4730	2008–2018	Semi-arid	
Arou	100.46°E, 38.05°N	Alpine meadow	3033	2008–2017	Sub-humid	Liu et al., 2011, 2018; Che et al., 2019
Dang-Xiong (DX)	91.06°E, 30.49°N	Alpine meadow	2957	2004–2010	Semi-arid	Yu et al., 2006;
Hai-Bei (HB)	101.32°E, 37.61°N	Alpine meadow	3190	2002–2010	Sub-humid	Zhang et al., 2019a

In the validation process, the half-hourly LE_{cor} data obtained from all the flux sites were subjected to further

processing, including conversion to daily and monthly averages, while employing a stringent quality control procedure. Daily values were set as null if they were derived from valid data points amounting to less than 80% in a single day. Similarly, monthly average values were disregarded in the validation if they were derived from valid data points accounting for less than 80% of observations for that month. This approach ensured the robustness of the validation process.

2.4 Accuracy metrics

The accuracy of the modeled ET was assessed by comparing the pixel values (M_i), corresponding to the latitude and longitude of the flux site, with the flux tower measurements (G_i). Several statistical metrics are employed for validation, including: (1) Coefficient of Determination (R^2): a measure of the proportion of the variance in the observed data (G_i) that is explained by the modeled data (M_i). A higher R^2 value indicates a stronger linear relationship between the two datasets. Mean Bias (*MB*) represents the average difference between the modeled *ET* (M_i) and the observed flux tower measurements (G_i). Positive *MB* values suggest overestimation by the model, while negative values indicate underestimation. Root Mean Square Error (*RMSE*): a measure of the standard deviation of the differences between modeled and observed values (M_i–G_i). A smaller RMSE implies greater accuracy in the model's predictions. Index of Agreement (*IOA*) indicates the degree of agreement between modeled and observed data, with a value of 1 indicating perfect agreement. Higher *IOA* values indicate better agreement between the two datasets. The equations for these parameters are as follows:

$$R^2 = \frac{\left(\sum_{i=1}^{n}(M_i-\overline{M})(G_i-\overline{G})\right)^2}{\sum_{i=1}^{n}(M_i-\overline{M})^2\sum_{i=1}^{n}(G_i-\overline{G})^2}, 0 \le R^2 \le 1 \quad (20)$$

$$MB = \frac{1}{N}\sum_{i=1}^{n}(M_i-G_i) \quad (21)$$

$$RMSE = \sqrt{\frac{1}{\mathrm{n}}\sum_{i=1}^{n}(M_i-G_i)^2} \quad (22)$$

$$IOA = 1-\frac{\sum_{i=1}^{n}(M_i-G_i)^2}{\sum_{i=1}^{n}(|M_i-\overline{G}|+|G_i-\overline{G}|)^2} \quad (23)$$

where the subscript *i* denotes individual samples, and *n* is the total number of samples used in the assessment. The significance of each parameter helps evaluate the model's performance in estimating *ET*.

3. Results

3.1 Evaluation of *ET* products against flux tower measurements

The reliability of remote sensing-based *ET* estimates is often in question without ground measurement verification. In this study, we compared the simulated monthly *ET* rates from the 0.05° grid where each *EC* site was located with the flux tower observational data to validate the MOD16-STM *ET* results. The validation outcomes for monthly MOD16-STM *ET*, using flux tower data, are illustrated in Fig. 4. The modeled *ET* exhibited excellent performance and high consistency across the TP when compared to *ET* observations.

Specifically, the grassland sites (SETORS, Arou, DX, and HB) displayed strong agreement, with R^2 and *IOA* values exceeding 0.82 and 0.95, respectively. The NAMORS site had the lowest performance, with the highest RMSE (17.84 mm/month) and the lowest R^2 and IOA (0.63 and 0.87, respectively). On average, the mean R^2 and IOA values exceeded 0.83 and 0.93, respectively. All R^2 values passed the significance test at the $p<0.05$ level. The mean |MB| and RMSE values were less than 3 mm/month^{1} and 14 mm/month. It's important to note that positive *MB* values indicated overestimation of *ET*, particularly during the dry season over barren land (QOMS, DX, SH, and NADORS) (Fig. 4). Conversely, underestimation occurred at higher *ET* rates in the summer, likely because the soil was close to saturation, leading to an overestimation of r_s^s and underestimation of E_s and *ET*. In general, the time series of *ET* variations at the nine flux tower stations exhibited clear seasonal and annual periodic variations (Fig. 5). The site-scale validation results demonstrate that MOD16-STM *ET* provides accurate estimates in the TP region.

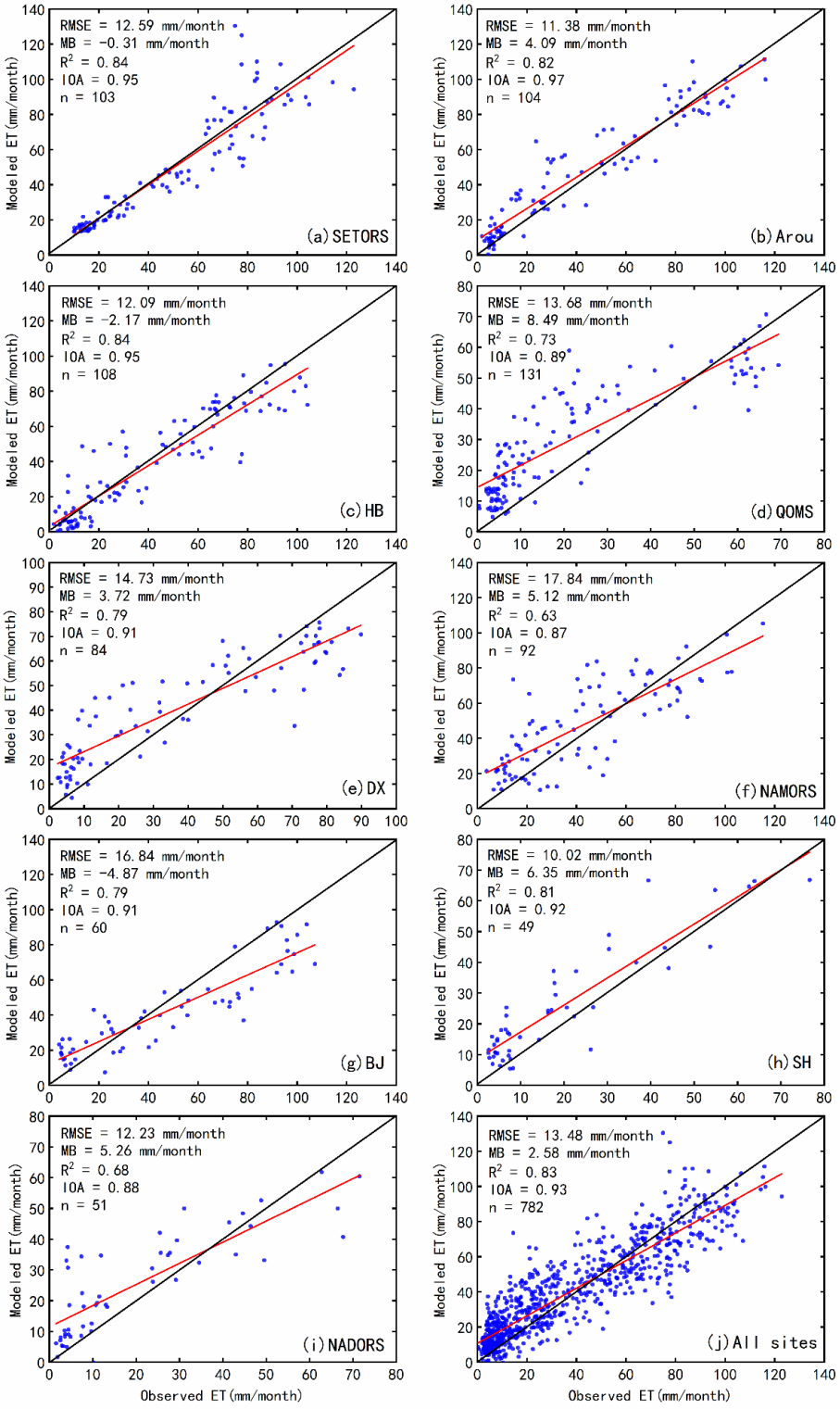

Figure 4 The validation of the MOD16-STM monthly ET at (a) SETORS, (b) Arou, (c) HB, (d) QOMS, (e) DX, (f) NAMORS, (g) BJ, (h) SH, (i) NADORS, and (j) all sites.

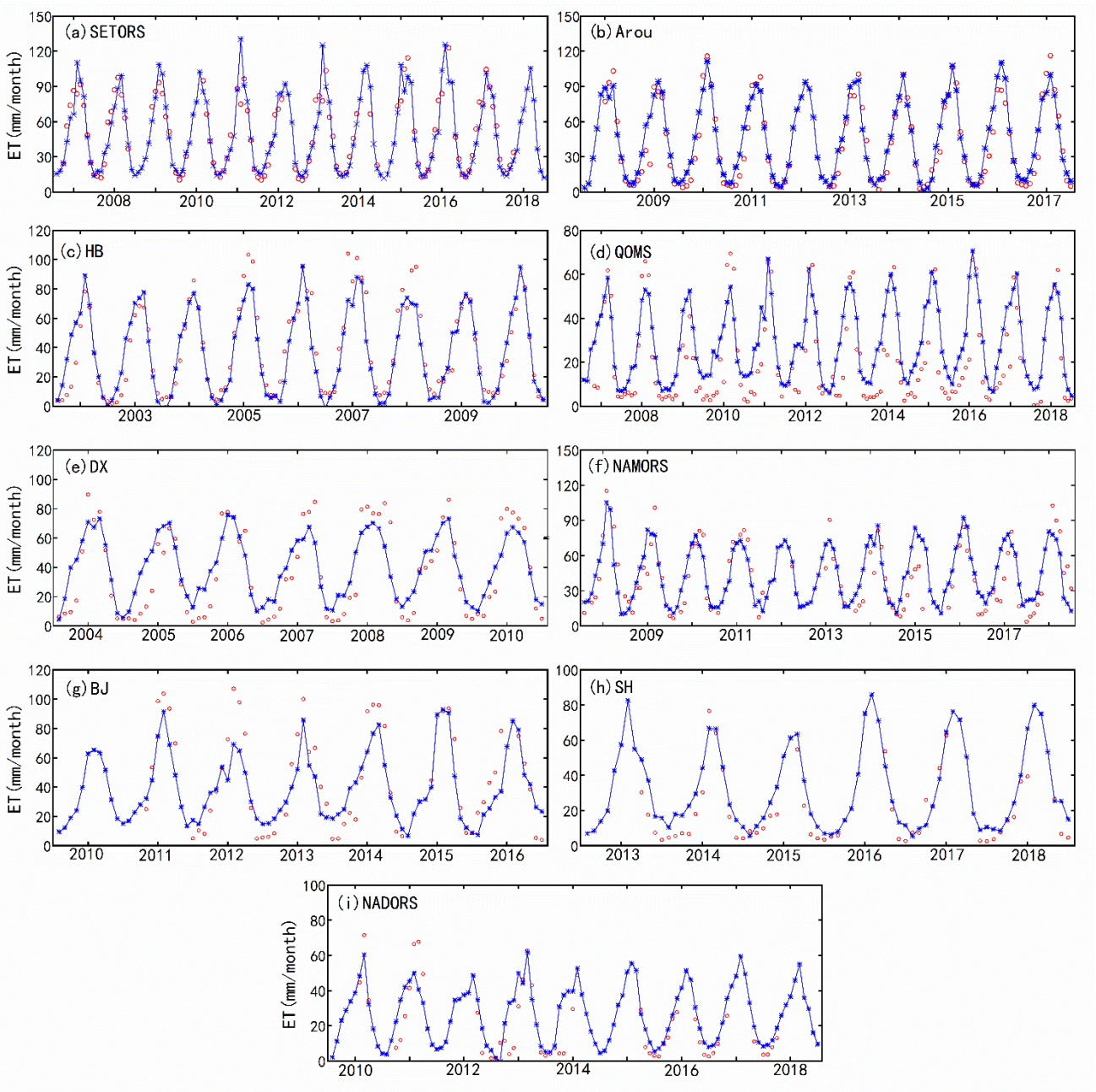

Figure 5 Time series variations in the MOD16-STM simulated ET (blue solid line with '*' marks) and flux-tower-observed ET (red circles) at (a) SETORS, (b) Arou, (c) HB, (d) QOMS, (e) DX, (f) NAMORS, (g) BJ, (h) SH, and (i) NADORS.

3.2 Spatial pattern of the multiyear averaged *ET* across TP

Figure 6 displays the spatial distribution of average annual *ET* and its three components across the TP. *ET* exhibited a decreasing trend from southeast to northwest, with the highest values exceeding 1000 mm/year in the southeastern TP (the Heng-duan Mountains) and the lowest values of less than 100 mm/year in the Qaidam Basin and northwestern TP. This spatial pattern of annual *ET* closely mirrored that of the aridity index (AI) (Fig.

1b), which is influenced by both atmospheric demand and water supply. The sub-humid zone, covering approximately 32.9% of the TP, contributed the highest proportion (43% of the TP's total *ET*) compared to other climate zones. E_s clearly dominated the central and western TP, with its spatial distribution closely resembling that of the overall *ET*. The spatial distributions of E_c and E_w are in line with the distribution of vegetation. High values of E_c (>200 mm/year) and E_w (>50 mm/year) are primarily concentrated in densely vegetated areas such as the Heng-duan Mountains in the southeastern TP.

The multi-year average *ET* for each season on the TP is depicted in Figure 6, covering spring (March, April, and May), summer (June, July, and August), autumn (September, October, and November), and winter (December, January, and February). The estimated *ET* reflects the general seasonal patterns quite accurately. During spring, the average *ET* was higher than in autumn, ranging from 20 to 250 mm/month in spring and from 20 to 150 mm/month in autumn. This difference can be attributed to the increase in surface water generated by the thawing of permafrost and the melting of snow and ice as temperatures rise in spring, which intensifies surface evaporation processes. Additionally, vegetation transpiration increases during the growing season. In summer, *ET* exceeds 200 mm/month over most of the TP, except for large areas in the northwestern TP where *ET* remains below 100 mm/month. Conversely, in winter, lower ET values are observed primarily in the densely vegetated southeastern region of the TP due to reduced water availability (precipitation) and lower T_a across the entire TP during this season.

Over the TP, the multi-year seasonal *ET* averages across the entire TP are as follows: 90.79±3.16 mm/year (0.23±0.0081 Gt/year) in spring, 152.05±8.44 mm/year (0.38±0.021 Gt/year) in summer, 71.96±2.86 mm/year (0.18±0.0074 Gt/year) in autumn, and 30.54±1.85 mm/year (0.077±0.0047 Gt/year) in winter. The multi-year average *ET* is 346.5±13.2 mm/year, representing both the mean and standard deviation, which characterizes interannual variability. This corresponds to approximately 0.88±0.034 Gt/year. Among its components, E_s accounted for 292.36±10.39 mm/year (0.74±0.027 Gt/year), E_c amounted to 47.85±3.34 mm/year (0.12±0.006 Gt/year), and E_w is 7.07±2.89 mm/year (0.02±0.001 Gt/year). Notably, E_s constituted the majority of *ET* on the TP, exceeding 84%. Wang et al. (2020) accurately estimated that the water evaporated from all plateau lakes was 0.0517 Gt/year. Therefore, utilizing the area-weighted average method, the annual average water evaporation across the entire TP was approximately 0.93±0.037 Gt/year. Furthermore, the TP has an average annual rainfall of about 1.8×10^3 Gt/year, estimated by Jiang et al. (2022). Remarkably, approximately 53% of the TP's precipitation returns to the atmosphere through *ET*.

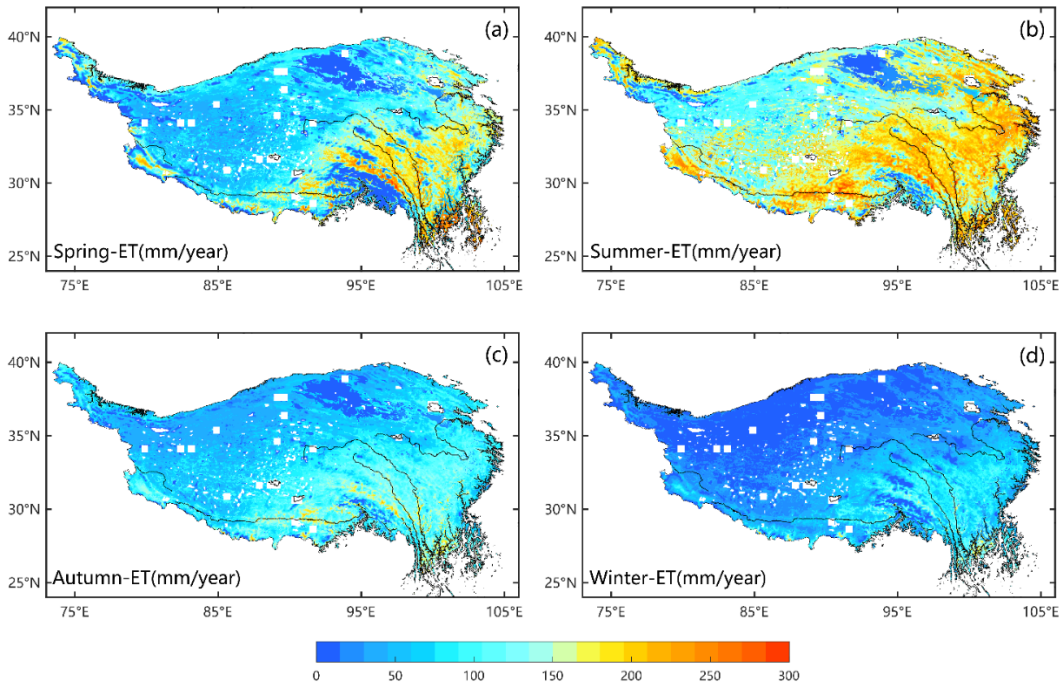

Figure 6 Spatial distributions of the multiyear (1982–2016) mean seasonal *ET* in (a) Spring, (b) Summer, (c) Autumn, and (d) Winter across the Tibetan Plateau.

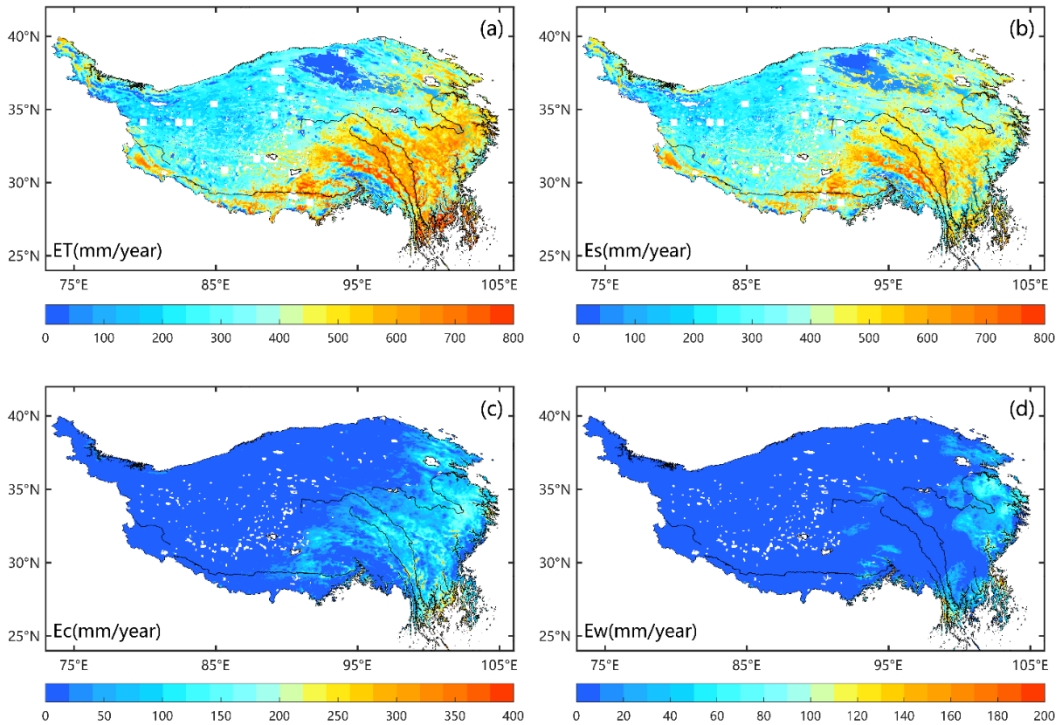

Figure 7 Spatial pattern of the multiyear (1982–2018) mean annual (a) *ET* (evapotranspiration), (b) E_s (soil evaporation), (c) E_c (canopy transpiration), and (d) E_w (intercepted water evaporation) across the Tibetan Plateau.

3.3 Temporal variations in *ET* across TP

Quantifying variations in *ET*, both inter- and intra-annual, holds significant importance in understanding monsoon phenomena and studying climate change patterns on the TP. Figure 8 presents the spatial distribution of annual *ET* and its component trends from 1982 to 2018. These trends exhibit spatial heterogeneity across the TP. The annual *ET* has seen a significant increase, with rates ranging from 1 to 4 mm/year (p<0.05), primarily in the central and eastern TP, encompassing more than 86% of the plateau. Conversely, there has been a notable decrease in annual *ET*, with rates ranging from −3 to −1 mm/year, in the northwestern TP. Similarly, the trends for E_s mirror those of *ET*, albeit with slightly lower magnitudes (1–3 mm/year, p<0.05). Both E_c and E_w have shown slight increasing trends of 0–2 mm/year (p<0.05). When averaged across the entire TP, *ET*, E_s, and E_c exhibited significant increases during the period from 1982 to 2018, with rates of 0.96 mm/year, 0.64 mm/year, and 0.44 mm/year, respectively (p<0.05; see Fig. 8). Seasonally, positive, and significant trends were observed in all seasons for *ET* (Fig. 9), with the strongest trends occurring in summer (0.46 mm/year). Furthermore, multi-source *ET* products indicate that most regions of the TP have exhibited consistent *ET* changes over the past 30 years (Yin et al., 2013; Peng et al., 2016; Wang et al., 2018; Ma et al., 2019; Wang et al., 2020; Li et al., 2021; Ma et al., 2022).

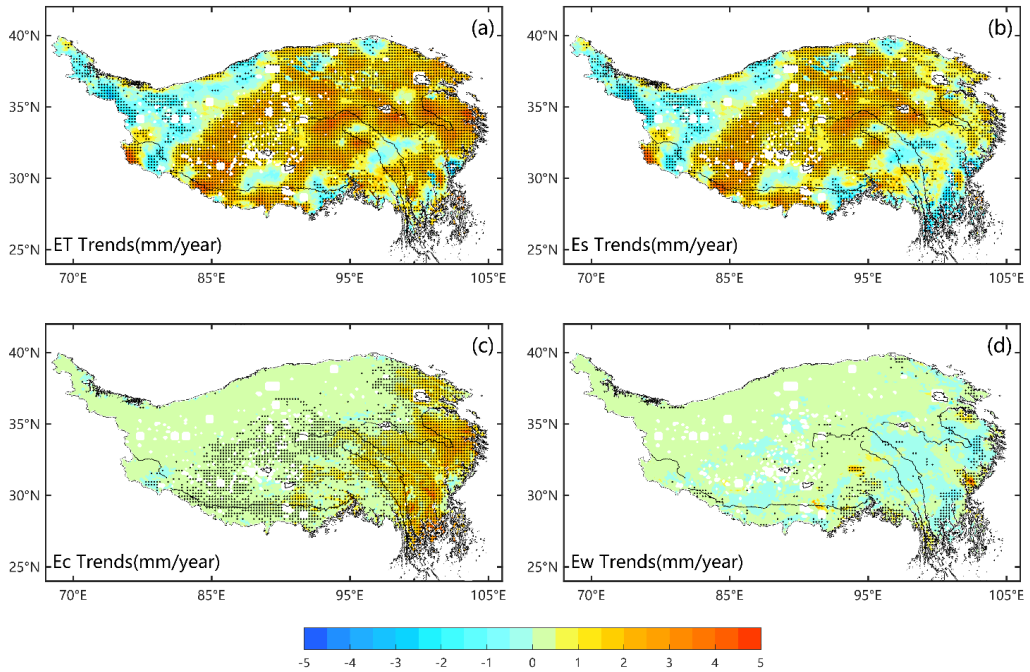

Figure 8 Spatial patterns of the trends (1982–2018) of the annual (a) *ET* (evapotranspiration), (b) E_s (soil evaporation), (c) E_c (canopy transpiration), and (d) E_w (intercepted water evaporation) across the Tibetan Plateau. The stippling on the maps indicates the trends that are statistically significant (p<0.05).

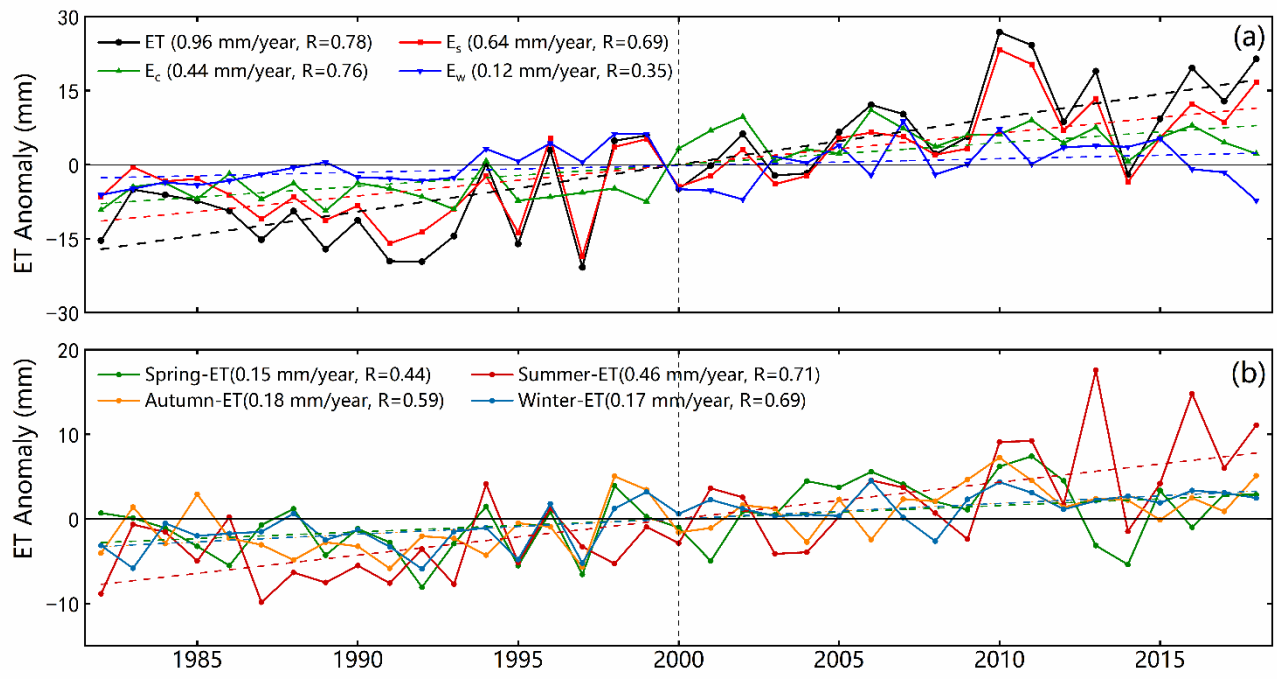

Figure 9 Time series of the (a) anomalies in the annual *ET* and its three components, and (b) anomalies in seasonal mean *ET*. The least squares fitted linear trend were demonstrated by the dashed colored lines.

The rise in *ET* across the entire TP from 1982 to 2018 can be attributed to the concurrent warming and increased precipitation experienced in this region during the same period. Since the 1980s, the TP has undergone a general trend of greening, warming, and heightened precipitation, as illustrated in Figure 10. *ET* has consistently increased over the past four decades, but there was a notable shift in climate factors around 2000. From 1982 to 2000, *ET* showed a continuous increase, accompanied by a rapid decline in wind speed, while the R_n remained relatively stable. However, between 2000 and 2018, there was a sharp decrease in R_n alongside an unchanged wind speed, but *ET* continued to rise during this period. Consequently, it is evident that R_n and wind speed were not the dominant factors driving annual variations in *ET*. The significant increases in T_a, *SM*, and precipitation have coincided with the greening of the land surface over the last two decades. These factors collectively contributed to the observed increase in *ET*. In the most recent decade, the substantial growth in *SM* emerged as the primary control factor for *ET* growth.

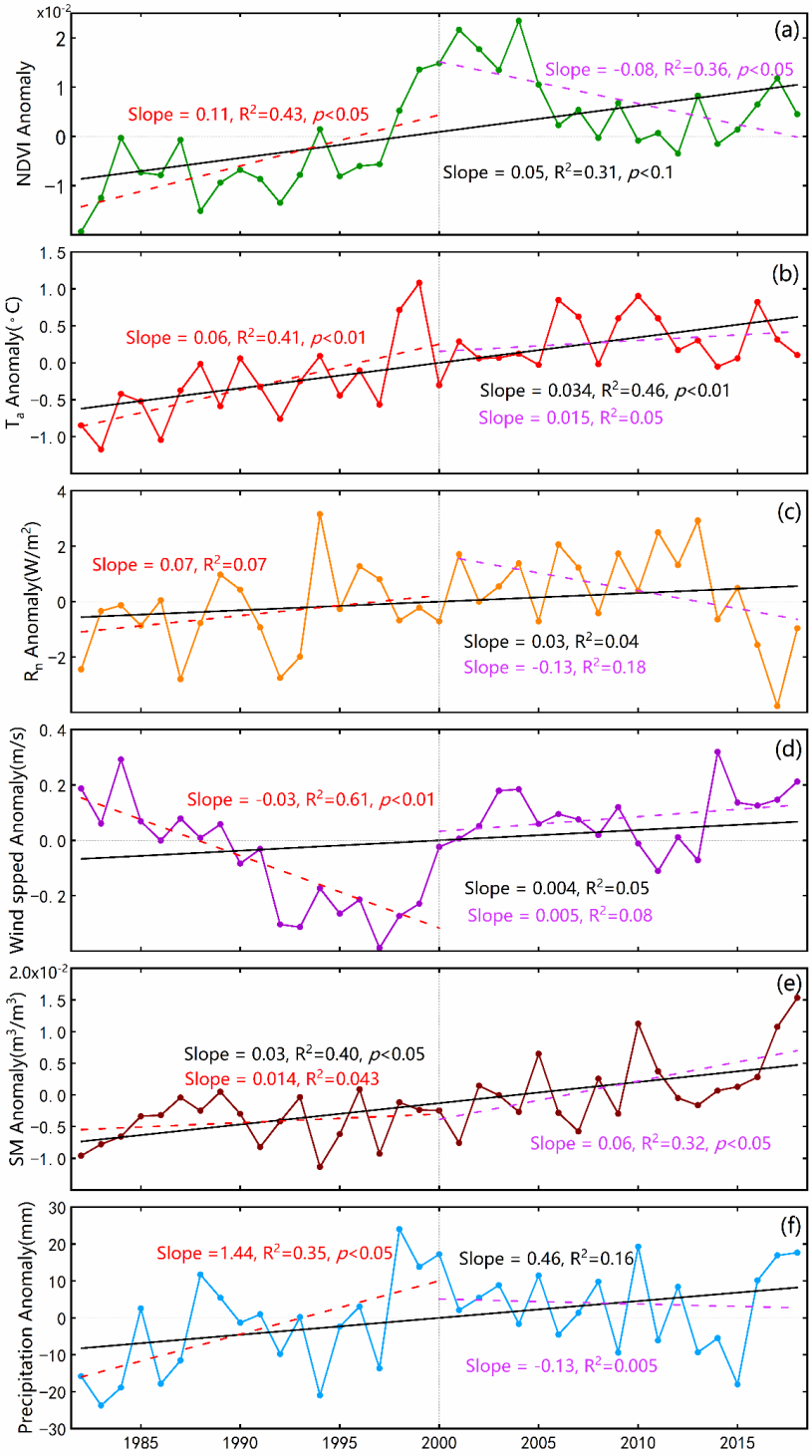

Figure 10 Time series of the annual anomalies in the (a) *NDVI*, (b) T_a, (c) R_n, (d) u, (e) *SM*, and (f) precipitation and their least squares fitted linear trends during two periods of 1982-2000 and 2000-2018.

In summary, the increase in *ET* over the TP can be attributed to multiple factors. Throughout the study period, the rise in available surface water played a significant role. Additionally, there is evidence of a general increase in precipitation across the TP (Fig. 10). The combined impact of warming (shown by T_a in Fig. 10) and

vegetation greening (shown by *NDVI* in Fig. 10) further facilitated the opening of vegetation stomata, promoting increased vegetation transpiration. The warming of the land surface and increased wind speeds enhanced the efficiency of turbulent water exchange between the land and atmosphere. Furthermore, land surface warming accelerated the melting of permafrost and glaciers on the TP. The surface wetting and the thickening of the active soil layer facilitated the transport of water from lower soil layers to upper layers. These environment changes, such as water availability, precipitation patterns, vegetation dynamics, temperature trends, all contributed to the increase in *ET* over the TP.

3.4 Comparison of the MOD16-STM product to other *ET* product over the TP

We have compared the accuracy of MOD16-STM product and other available dataset for the TP region. It is shown by Fig. 11. The MOD16-STM *ET* model demonstrated a high performance on the TP, with an average R^2 value of 0.87 and an average RMSE of 13.48 mm/month. Wang et al. (2018) evaluated a modified PML model for *ET* estimation on the TP, reporting R^2 values exceeding 0.85 and RMSE values lower than 14 mm/month. The spatially averaged *ET* for the period 1982–2012 was 378.1 mm/year. Wang et al. (2020) assessed the performance of the generalized nonlinear complementary principle for *ET* estimation based on flux tower observations from the TP. Their results indicated a R^2 of 0.93 and a RMSE 0.40 mm/day. The spatially averaged *ET* during 1982–2014 was 398.3 mm/year. Han et al. (2021) used a combination of the effective aerodynamic roughness length and the surface energy balance model to estimate *ET* for the entire TP from 2001 to 2018 (Han-ET). They found good agreement between modeled, and in-situ measured values ($R^2 > 0.81$, *RMSE* <14.5 mm/month), and the average annual *ET* was approximately 496±23 mm, which is higher than the 346.5±13.2 mm obtained in this study (Fig. 12). The discrepancy can be attributed to differences in models and time periods used in the two studies. Additionally, Ma et al. (2022) employed the PML_V2 model to estimate *ET* on the TP (PML), yielding R^2 and *RMSE* values ranging from 0.4 to 0.9 and from 0.3 to 0.8 mm/day, respectively. The 35-year mean annual *ET* rates from PML-Ma resulted in an average value of 353±24 mm/year for the entire TP. Notably, the proportion of soil evaporation estimated by PML-Ma was approximately 64% of the total *ET*, which is lower than the estimated 84% in this study. The primary reason for this difference may be attributed to variations in land cover classification. The MODIS land cover classification largely categorizes the land surface in the northwestern TP as bare soil, which in turn increases the proportion of soil evaporation.

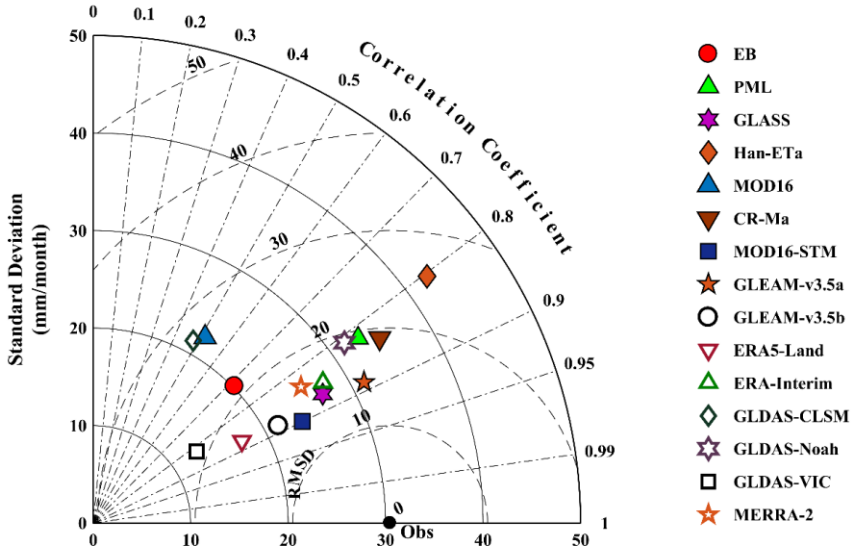

Figure 11. Taylor diagram of the monthly-scale evapotranspiration dataset validated with flux evapotranspiration observations.

4. Discussions

4.1 Discrepancy on the estimation of annual *ET* over the TP

Figure 12 provides a comprehensive overview of the time periods covered by various *ET* datasets and their annual *ET* estimations for the TP. Yao et al. (2013) estimated TP's *ET* (PT-Yao) in China using a satellite-driven modified Priestley–Taylor algorithm, constrained by *NDVI* and apparent thermal inertia derived from temperature changes over time. Their reported mean annual *ET* for the TP was approximately 320 mm/year. Song et al. (2017) estimated TP's *ET* (PM-Song) from 2000 to 2010 using the improved Penman–Monteith method along with meteorological and satellite remote sensing data at a 1 km spatial resolution. They concluded that the average annual *ET* on the TP was 350.3 mm/year. Additionally, 18 mean annual *ET* values estimated using existing *ET* products (PML-Zhang (Zhang et al., 2019b), EB-*ET* (Chen et al., 2019), CR-Ma (Ma et al., 2019), CMIP6-ssp126 (Eyring et al., 2016), GLDAS-Noah (Rodell et al., 2004), GLASS (Liang et al., 2021), GLEAM-v3.5b (Miralles et al., 2011, 2016), ERAR-Land (Muñoz-Sabater et al., 2021), MTE (Jung et al., 2010), PM-Li (Li et al., 2014a, 2014b), LPJ-Yin (Yin et al., 2013)) were included for comparison. Among these, Han-ET, ERA5-Land, and CMIP6 produced the highest values (>400 mm/year, while LPJ-Yin, GLASS, EB-*ET*, GLDAS, and GLEAM values were less than 300 mm/year. The results demonstrate substantial variability in the estimated mean annual *ET* values for the TP. These differences are influenced by objective factors such as data accuracy, limitations of validation method, and algorithm flaws. The ensemble mean of all datasets yields an

annual *ET* of 348.6 mm/year, with the MOD16-STM model's estimation (346.5 mm/year) being the closest to this ensemble mean. Overall, the MOD16-STM *ET* model demonstrated acceptable performance on the TP once again.

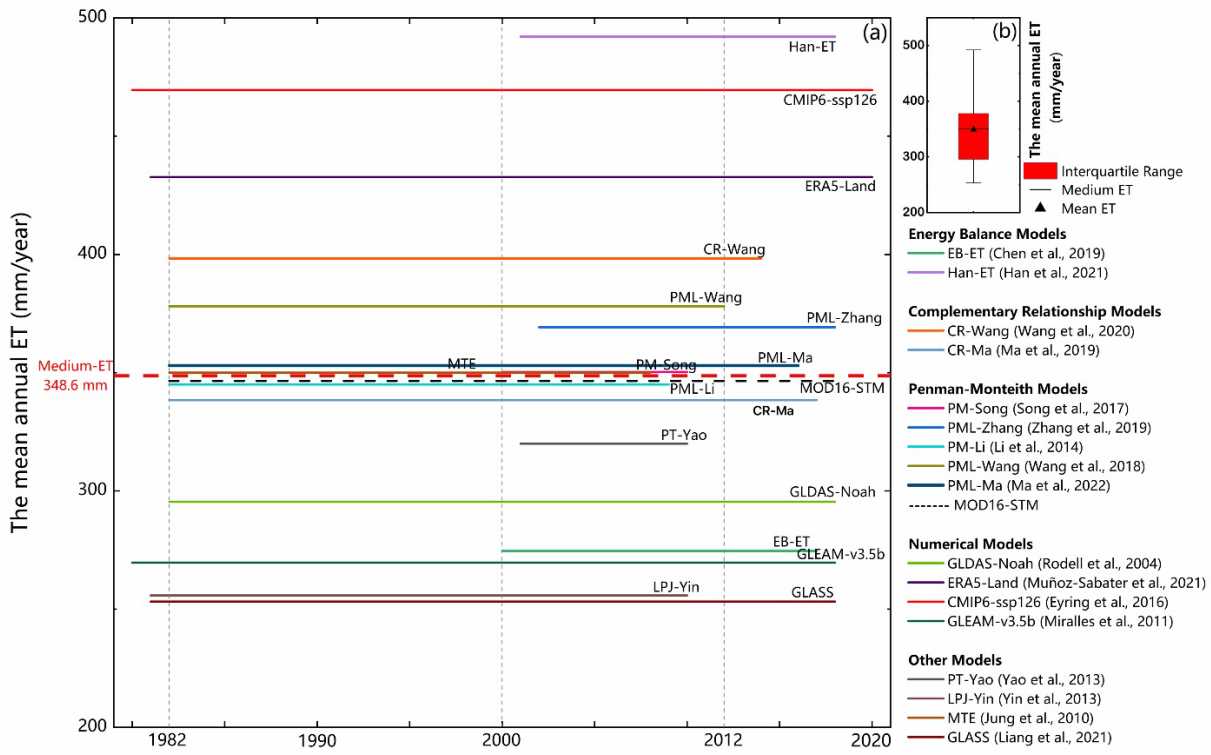

Figure 12 (a) The annual mean *ET* values of 18 datasets. The *x*-axis is the time coverage of the *ET* datasets, and the *y*-axis is the multi-year mean value. (b) The bars denote the mean values and variations of the annual *ET*.

4.2 Errors caused by objective factors

The MOD16-STM model, along with other models, relies on remote sensing and reanalysis data as its primary input data sources. However, it's important to acknowledge the inherent uncertainty in these datasets (Ramoelo et al., 2014). For example, the topsoil water content from satellite data includes some errors (Liu et al. 2021). This indicates that SM from GLEAM may introduce uncertainties to our *ET* estimation. Some studies have documented the greening of the TP. Figure 10a demonstrated a significant decrease in *NDVI* after 2000, which contrasts with the *NDVI* changes reported by Wang et al. (2022). This inconsistency highlights the considerable uncertainty in the *NDVI* data. Additionally, *LST* plays a fundamental role in the calculation of the surface energy balance and, consequently, errors in ERA5 *LST* can also bring uncertainty to the *ET* estimation. In this study, a threshold value of *NDVI* (0.25) was used to categorize land surface as either bare soil or canopy-covered pixels. This threshold value may miss-classify bare soil and grassland on the TP. The land cover

mismatches between the reality and the land surface types in the MOD16-STM *ET* model can also introduce errors in the model simulation.

It is worth noting that flux towers used for validation typically cover areas ranging from a few hundred square meters to several square kilometers. These validation sites' representativeness depends on factors such as observation instrument height, turbulence intensity, topography, environment, and vegetation conditions. While site-scale evaluations of the MOD16-STM *ET* are conducted in this study, it's essential to recognize the uncertainties stemming from the limited number of validation sites. Future research should consider validation across various land cover types, climate zones, elevations, and seasons to provide a more comprehensive assessment of model performance.

While the MOD16 model provides a direct estimation of *ET*, bypassing the need for calculating sensible heat, it still relies on empirical coefficients, particularly those redefined for different soil textures. However, there are remaining empirical parameters, such as C_L (the mean potential stomatal conductance per unit leaf area), which can introduce uncertainties into simulation results. Thus, future studies should prioritize the parameterization of these empirical factors based on physical processes to reduce simulation uncertainties. It's crucial to consider the influence of physical processes related to deeper soil water and heat transfer on resistance. The MOD16-STM algorithm's accuracy is highly dependent on higher-precision soil moisture products. Given that a substantial portion of the TP is covered by permafrost and seasonally frozen soil, it becomes challenging to assess soil moisture conditions during freezing and thawing periods. Consequently, it is essential to employ observations during freeze-thaw periods to validate the model's applicability.

In summary, enhancing the model by incorporating physical parameterizations, especially for empirical coefficients, and accounting for the complexities of soil moisture variations in frozen regions will contribute to reducing uncertainties in *ET* simulation results in future research.

5. Conclusion

In this study, we have developed a 37-year (1982–2018) monthly *ET* dataset with a high spatial resolution (0.05°) for the TP using the newly developed MOD16-STM model. This dataset covers the entire study area with both high spatial resolution and a long time series, making it a valuable resource for climate studies. Then we investigated the spatial distribution and temporal trends of *ET* across the TP. Key findings are summarized below:

- The *ET* product generated by the MOD16-STM model exhibited strong performance on the TP. When

compared to flux tower observation data, the model achieved high R^2 and *IOA* values of 0.83 and 0.93, respectively, with an *RMSE* of 13.48 mm/month and a modest bias (*MB*) of 2.58 mm/month. This *ET* dataset holds potential applications in water resource management, drought monitoring, and ecological studies.

- The *ET* on the TP displayed spatial heterogeneity and temporal variations driven by a combination of atmospheric demand and water supply. Generally, annual *ET* decreased from the southeastern to the northwestern regions of the TP. E_s accounted for over 84% of the annual *ET*, and the estimated multi-year mean annual *ET* on the TP for the period 1982–2018 was 346.5±13.2 mm. This corresponds to an annual water evaporation of about 0.93±0.037 Gt from the entire TP.
- Significant temporal trends were observed in the *ET*. Most parts of the central and eastern TP exhibited increasing trends of about 1 to 4 mm/year (p<0.05), whereas the northwestern TP showed a decreasing trend of −3 to −1 mm/year (p<0.05). Averaged across the entire TP, the *ET* increased significantly at a rate of 0.96 mm/year (p<0.05) during the period 1982–2018. This increase in *ET* over the entire TP from 1982 to 2018 can be attributed to the warming and wetting of the climate during this period.

These findings contribute to a better understanding of the *ET* dynamics on the Tibetan Plateau and provide a valuable dataset for climate research and related applications.

Data availability

The monthly ET dataset presented and analyzed in this article has been released and is freely available at the Science Data Bank (http://doi.org/10.11922/sciencedb.00020, Y. Ma*, X.Chen*, L. Yuan, 2021) and the National Tibetan Plateau Data Center (TPDC) (https://data.tpdc.ac.cn/en/disallow/e253621a-6334-4ad1-b2b9-e1ce2aa9688f/, http://doi.org/10.11888/Terre.tpdc.271913, L. Yuan, X.Chen*, Y. Ma*, 2021). The dataset is published under the Creative Commons Attribution 4.0 International (CC BY 4.0) license.

Author contributions

YMM, LY, and XLC led the writing of this paper and acknowledge responsibility for the experimental data and results. LY, XLC and YMM drafted the paper, and LY led the consolidation of the input and simulation dataset. XLC revised the manuscript. This paper was written in cooperation with all the co-authors.

Declaration of Competing Interest

The authors declare that they have no known competing financial interests or personal relationships that

could have appeared to influence the work reported in this paper.

Acknowledgments

We are grateful for the datasets provided by the China-Flux (http://www.chinaflux.org/), Ameri-Flux (https://ameriflux.lbl.gov/), GHG-Europe (http://www.europe-fluxdata.eu/ghg-europe), the National Tibetan Plateau Data Center (https://data.tpdc.ac.cn/zh-hans/data), the European Centre for Medium-Range Weather Forecasts (ECWMF) (https://www.ecmwf.int/), NOAA-NCEI (https://www.ncei.noaa.gov/products/climate-data-records/normalized-difference-vegetation), the Global Land Evaporation Amsterdam Model (https://www.gleam.eu/), and the National Earth System Science Data Sharing Infrastructure (http://glass-product.bnu.edu.cn/). The authors would like to thank all their colleagues at the observation stations on the TP for their maintenance of the instruments.

Financial support

This study was funded by the Second Tibetan Plateau Scientific Expedition and Research (STEP) Program (2019QZKK0103 and 2019QZKK0105), and the National Natural Science Foundation of China (42230610, 91837208, 41975009).

Appendix A: MOD16-STM model validation at flux site out of the Tibetan Plateau

Table A1. Basic information about the five test sites (which is used to test the relationship between soil surface resistance (r_s^s) and SM/θ_{sat} in the MOD16-STM model) and 12 verification sites (used for the MOD16-STM model evaluation at site scale). All the stations are locating outside of the Tibetan Plateau.

	Site	Lat; lon	Land cover	θ (cm)	f_{sand}	f_{clay}	m_{soc} (%)	θ_{sat}	Soil Texture	Reference
Test Sites	IT-Cas	45.07; 8.71	CRO	5	0.28	0.29	2.6	/	Clay loam	*Denef et al. (2013)*
	US-IHO	36.47; 100.62	Bare	5	0.58	0.28	/	0.53	Sandy Clay Loam	*Lemone et al*. (2007)
	US-Arm	36.61; -97.49	CRO	5	0.28	0.43	1.5	/	Clay	*Fischer et al*. (2007)
	CH-Oe2	47.29; 7.73	CRO	5	0.095	0.43	2.8	/	Silty Clay	*Alaoui and Goetz* (2008)
	US-IB2	41.84; -88.24	GRA	0~15	0.106	0.29	2.4	/	Silty clay Loam	/
Verification sites	US-Dk1	35.97; -79.09	GRA	10	0.48	0.09	/	0.52	Loam	*Novick et al. (2004)*
	US-Fwf	35.45; -111.77	GRA	5	0.30	0.13	3.2	/	Silt Loam	*Dore et al. (2012)*
	US-Wkg	31.74; -109.94	GRA	5	0.67	0.17	1.0	/	Sandy Loam	*Ameri-Flux*
	CA-Obs	53.98; -105.11	ENF	5	0.72	0.05	4.3	/	Sandy Loam	*Ameri-Flux*
	CA-Ojp	53.91; -104.69	ENF	5	0.94	0.03	2.5	/	Sand	*Ameri-Flux*
	CA-Ca2	49.87; -125.29	ENF	5	0.74	0.03	3.0	/	Loamy Sand	*Ameri-Flux*
	CA-Ca3	49.53; -124.90	ENF	5	0.39	0.20	4.9	/	Loam	*Ameri-Flux*
	US-Dk3	35.97; -79.09	ENF	5	0.25	0.34	2.4	/	Silt Loam	*Ameri-Flux*
	US-Fuf	35.08; -111.76	ENF	5	0.31	0.35	3.9	/	Clay Loam	*Ameri-Flux*
	US-Ib1	41.86; -88.22	CRO	2.5	0.10	0.35	1.8	/	Silty clay Loam	*Denef et al. (2013)*
	ES-ES2	39.28; -0.32	CRO	5	0.11	0.47	3.7	/	Silty Clay	*Kutsch et al. (2010)*
	IT-Bci	40.52; 14.96	CRO	5	0.32	0.46	1.5	/	Clay	*Denef et al. (2013)*

Table A2. Assessment results of the daily *ET* (mm/day) simulated by the MOD16-STM model at the 12 verification sites. This simulation is driven by the in-situ meteorological observation data.

	Sites	R^2 (p<0.05)	*IOA*	|*MB*|	*RMSE*
Grassland	US-DK1	0.71	0.91	0.27	0.74
	US-Fwf	0.59	0.84	0.06	0.55
	US-Wkg	0.69	0.84	0.005	0.58
Evergreen Forest	CA-Obs	0.88	0.96	0.05	0.33
	CA-Ojp	0.79	0.93	0.11	0.38
	CA-Ca2	0.77	0.92	0.23	0.49
	CA-Ca3	0.79	0.94	0.02	0.44
	US-Dk3	0.79	0.92	0.51	0.87
	US-Fuf	0.58	0.81	0.33	0.66
Cropland	US-Ib1	0.65	0.88	0.39	1.08
	ES-ES2	0.87	0.91	0.04	0.94
	IT-Bci	0.41	0.76	0.14	1.14
Mean	/	0.72	0.89	0.18	0.68

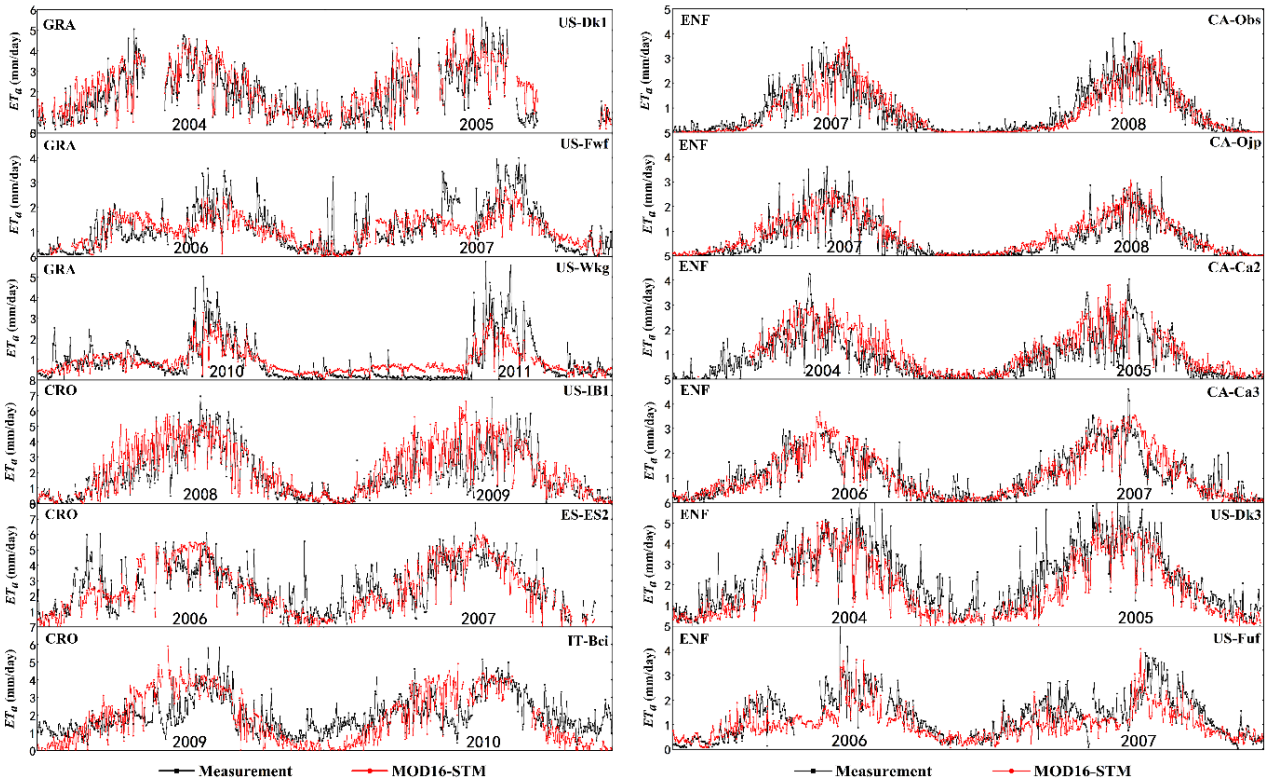

Figure A1. Time-series comparisons of the daily *ET* estimated by the MOD16-STM model and observations at the 12 verification sites, which include three grassland sites (US-DK1, US-Fwf, and US-Wkg), three cropland sites (US-IB1, ES-ES2, and IT-Bci), and six evergreen forest sites (CA-Obs, CA-Ojp, CA-Ca2, CA-Ca3, US-DK3, and US-Fuf) respectively.

596 **References**

597 Alaoui, A., and Goetz, B.: Dye tracer and infiltration experiments to investigate macropore flow, Geoderma.,
598 144(1–2), 279–286, https://doi.org/10.1016/j.geoderma.2007.11.020, 2008.

599 Baik, J., Liaqat, U. W., and Choi, M.: Assessment of satellite- and reanalysis-based evapotranspiration products
600 with two blending approaches over the complex landscapes and climates of Australia, Agric. For. Meteorol.,
601 263, 388–398. https://doi.org/10.1016/j.agrformet.2018.09.007, 2018.

602 Bibi, S., Wang, L., Li, X., Zhou, J., Chen, D., Yao, T.: Climatic and associated cryospheric, biospheric, and
603 hydrological changes on the Tibetan Plateau: a review, Int. J. Climatol., 38, 1-17,
604 https://doi.org/10.1002/joc.5411, 2018.

605 Biermann, T., Babel, W., Ma, W., Chen, X., Thiem, E., Ma, Y., Foken, T.: Turbulent flux observations and
606 modelling over a shallow lake and a wet grassland in the Nam Co basin, Tibetan Plateau, Theor. Appl.
607 Climatol., 116(1–2), 301–316, https://doi. org/10.1007/s00704-013-0953-6, 2014.

608 Blyth, E., and Harding, R. J.: Methods to separate observed global evapotranspiration into the interception,
609 transpiration, and soil surface evaporation components, Hydrol. Process., 25(26), 4063–4068,
610 https://doi.org/10.1002/hyp.8409, 2011.

611 Camillo, P. J. and Gurney, R. J.: A resistance parameter for bare soil evaporation models, Soil Sci., 141(2), 95–
612 105, https://doi.org/10.1097/00010694-198602000-00001, 1986.

613 Chang, Y., Qin, D., Ding, Y., Zhao, Q., Zhang, S: A modified MOD16 algorithm to estimate evapotranspiration
614 over alpine meadow on the Tibetan Plateau, China, J. Hydrol., 561: 16–30,
615 https://doi.org/10.1016/j.jhydrol.2018.03.054, 2018.

616 Chen, X., Massman, W. J., Su, Z.: A Column Canopy-Air Turbulent Diffusion Method for Different Canopy
617 Structures, J. Geophys. Res. Atmos., 124(2), 488–506, https://doi.org/10.1029/2018JD028883, 2019.

618 Chen, X., Su, Z., Ma, Y., Liu, S., Yu, Q., Xu, Z.: Development of a 10-year (2001–2010) 0.1° data set of land-
619 surface energy balance for mainland China, Atmos. Chem. Phys., 14(23), 13097–13117,
620 https://doi.org/10.5194/acp-14-13097-2014, 2014.

621 Chen, X., Su, Z., Ma, Y., Yang, K., Wen, J., Zhang, Y.: An Improvement of Roughness Height Parameterization
622 of the Surface Energy Balance System (SEBS) over the Tibetan Plateau, J. Appl. Meteorol. Climatol.,
623 52(3), 607–622, https://doi.org/10.1175/JAMC-D-12-056.1, 2013.

624 Chen, X., Su, Z., Ma, Y., Trigo, I., Gentine, P.: Remote Sensing of Global Daily Evapotranspiration based on a
625 Surface Energy Balance Method and Reanalysis Data, J. Geophys. Res. Atmos., 126(16), e2020JD032873,

https://doi.org/10.1029/2020JD032873, 2021.

Chen, Y., Xia, J., Liang, S., Feng, J., Fisher, J. B., Li, X., Li, X., Liu, S., Ma, Z., Miyata, A., Mu, Q., Sun, L., Tang, J., Wang, K., Wen, J., Xue, Y., Yu, G., Zha, T., Zhang, L., Zhang, Q., Zhao, T., Zhao, L., Yuan, W.: Comparison of satellite-based evapotranspiration models over terrestrial ecosystems in China, Remote Sens. Environ., 140, 279–293, https://doi.org/10.1016/j.rse.2013.08.045, 2014.

Chen, Y., Yang, K., Tang, W., Qin, J., and Zhao, L.: Parameterizing soil organic carbon's impacts on soil porosity and thermal parameters for Eastern Tibet grasslands, Sci. China Earth Sci., 55(6), 1001–1011, https://doi.org/10.1007/s11430-012-4433-0, 2012.

Che, T., Li, X., Liu, S., Li, H., Xu, Z., Tan, J., Zhang, Y., Ren, Z., Xiao, L., Deng, J., Jin, R., Ma, M., Wang, J., and Yang, X.: Integrated hydrometeorological, snow and frozen-ground observations in the alpine region of the Heihe River Basin, China, Earth Syst. Sci. Data., 11, 1483–1499, https://doi.org/10.5194/essd-11-1483-2019, 2019.

Cosby, B. J., Hornberger, G. M., Clapp, R. B., and Ginn, T. R.: A Statistical Exploration of the Relationships of Soil Moisture Characteristics to the Physical Properties of Soils, Water Resour. Res., 20(6), 682–690, https://doi.org/10.1029/WR020i006p00682, 1984.

Dan, J., Gao, Y., and Zhang, M.: tecting and Attributing Evapotranspiration Deviations Using Dynamical Downscaling and Convection-Permitting Modeling over the Tibetan Plateau, Water., 13(15), 2096: https://doi.org/10.3390/w13152096, 2017.

De Kok, R.J., Kraaijenbrink, P.D.A., Tuinenburg, O.A., Bonekamp, P.N.J., Immerzeel, W.W.: Towards understanding the pattern of glacier mass balances in High Mountain Asia using regional climatic modelling, Cryosphere, 14, 3215–3234, https://doi.org/10.5194/tc-14-3215-2020, 2020.

Denef, K., Galdo, I. D., Venturi, A., and Cotrufo, M. F.: Assessment of Soil C and N Stocks and Fractions across 11European Soils under Varying Land Uses, Open J. Soil Sci., 03(07), 297–313, https://doi.org/10.4236/ojss.2013.37035, 2013.

Dore, S., Montes-Helu, M., Hart, S. C., Hungate, B. A., Koch, G. W., Moon, J. B., Finkral, A., Kolb, T. E.: Recovery of ponderosa pine ecosystem carbon and water fluxes from thinning and stand-replacing fire, Glob. Chang. Biol., 18(10), 3171–3185, https://doi.org/10.1111/j.1365-2486.2012.02775.x, 2012.

Ding, J., Chen, L., Ji, C., Hugelius, G., Li, Y., Liu, L., Qin, S., Zhang, B., Yang, G., Li, F., Fang, K., Chen, Y., Peng, Y., Zhao, X., He, H., Smith, P., Fang, J., Yang, Y.: Decadal soil carbon accumulation across Tibetan permafrost regions, Nature Geoscience, 10(6), 420–424, https://doi.org/10.1038/ngeo2945, 2017.

656 Eyring, V., Bony, S., Meehl, G. A., Senior, C. A., Stevens, B., Stouffer, R. J., Taylor, K. E.: Overview of the
657 Coupled Model Intercomparison Project Phase 6 (CMIP6) experimental design and organization, Geosci.
658 Model Dev., 9, 1937–1958. https://doi.org/10.5194/gmd-9-1937-2016, 2016.
659 Farouki, O.T.: The thermal properties of soils in cold regions, Cold Reg. Sci., Technol. 5, 67–75,
660 https://doi.org/10.1016/0165-232X(81)90041-0, 1981.
661 Fischer, M. L., Billesbach, D. P., Berry, J. A., Riley, W. J., and Torn, M. S.: Spatiotemporal variations in
662 growing season exchanges of CO2, H2O, and sensible heat in agricultural fields of the Southern Great
663 Plains, Earth Interact., 11(17), https://doi.org/10.1175/EI231.1, 2007.
664 Gan, R., Zhang, Y., Shi, H., Yang, Y., Eamus, D., Cheng, L., Chiew, F., Yu, Q.: Use of satellite leaf area index
665 estimating evapotranspiration and gross assimilation for Australian ecosystems, Ecohydrology, 11(5),
666 e1974, https://doi.org/10.1002/eco.1974, 2018.
667 Good, S. P., Noone, D., and Bowen, G.: Hydrologic connectivity constrains partitioning of global terrestrial
668 water fluxes, Science, 349(6244), 175–177, https://doi.org/10.1126/science.aaa5931, 2015.
669 Han, C., Ma, Y., Chen, X., Su, Z.: Trends of land surface heat fluxes on the Tibetan Plateau from 2001 to 2012,
670 Int. J. Climatol., 37, 4757–4767, https://doi.org/10.1002/joc.5119, 2017.
671 Han, C., Ma, Y., Wang, B., Zhong, L., Ma, W., Chen, X., and Su, Z.: Long term variations of actual
672 evapotranspiration over the Tibetan Plateau, Earth Syst. Sci. Data., 13, 3513–3524,
673 https://doi.org/10.5194/essd-13-3513-202, 2021.
674 He, J., Yang, K., Tang, W., Lu, H., Qin, J., Chen, Y., Li, X.: The first high-resolution meteorological forcing
675 dataset for land process studies over China, Sci. Data., 7(1), 25, https://doi.org/10.1038/s41597-020-0369-
676 y, 2020.
677 Immerzeel, W. W., Van Beek, L. P. H., Bierkens, M. F. P.: Climate change will affect the Asian water towers.
678 Science, 2010, 328(5984), 1382–1385. https://doi.org/10.1126/science.1183188
679 Immerzeel, W. W., Lutz, A. F., Andrade, M., Bahl, A., Biemans, H., Bolch, T., Hyde, S., Brumby, S., Davies,
680 B., Elmore, A., Emmer, A., Feng, M., Fernández, A., Haritashya, U., Kargel, J., Koppes, M., Kraaijenbrink,
681 P., Kulkarni, A., Mayewski, P., Nepal, S., Pacheco, P., Painter, T., Pellicciotti, F., Rajaram, H., Rupper, S.,
682 Sinisalo, A., Shrestha, A., Viviroli, D., Wada, Y., Xiao, C., Yao, T., Baillie, J. E. M.: Importance and
683 vulnerability of the world's water towers, Nature, 577(7790), 364–369, https://doi.org/10.1038/s41586-
684 019-1822-y, 2020.
685 Irmak, S., and Mutiibwa, D.: On the dynamics of canopy resistance: Generalized linear estimation and

686 relationships with primary micrometeorological variables, Water Resour. Res., 46(8), W08526,
687 https://doi.org/10.1029/2009WR008484, 2010.
688 Jarvis, P. G.: The InterprETtion of the Variations in Leaf Water Potential and Stomatal Conductance Found in
689 Canopies in the Field. Philos, Trans. R. Soc. London. B, Biol. Sci., 273(927), 593–610,
690 https://doi.org/10.1098/rstb.1976.0035, 1976.
691 Jiang, Y., Yang, K., Qi, Y., Zhou, X., He, J., Lu, H., Li, X., Chen, Y., Li, X., Zhou, B., Mamtimin, A., Shao, C.,
692 Ma, X., Tian, J., and Zhou, J.: TPHiPr: a long-term (1979–2020) high-accuracy precipitation dataset (1/
693 30°, daily) for the Third Pole region based on high-resolution atmospheric modeling and dense
694 observations, Earth Syst. Sci. Data, 15, 621–638, https://doi.org/10.5194/essd-15-621-2023, 2023.
695 Jung, M., Reichstein, M., Ciais, P., Seneviratne, S. I., Sheffield, J., Goulden, M. L., Bonan, G., Cescatti, A.,
696 Chen, J., De Jeu, R., Dolman, A., Eugster, W., Gerten, D., Gianelle, D., Gobron, N., Heinke, J., Kimball,
697 J., Law, B., Montagnani, L., Mu, Q., Mueller, B., Oleson, K., Papale, D., Richardson, A., Roupsard, O.,
698 Running, S., Tomelleri, E., Viovy, N., Weber, U., Williams. C., Wood, E., Zaehle, S., Zhang, K.: Recent
699 decline in the global land evapotranspiration trend due to limited moisture supply, Nature, 467(7318), 951–
700 954, https://doi.org/10.1038/nature09396, 2010.
701 Khan, M. S., Liaqat, U. W., Baik, J., and Choi, M.: Stand-alone uncertainty characterization of GLEAM,
702 GLDAS and MOD16 evapotranspiration products using an extended triple collocation approach, Agric.
703 For. Meteorol., 252, 256–268, https://doi.org/10.1016/j.agrformet.2018.01.022, 2018.
704 Kuang, X., and Jiao, J. J.: Review on climate change on the Tibetan plateau during the last half century, J.
705 Geophys. Res. Atmos., 121, 3979-4007, https://doi.org/10.1002/2015JD024728, 2016.
706 Kutsch, W. L., Aubinet, M., Buchmann, N., Smith, P., Osborne, B., Eugster, W., Wattenbach, M., Schrumpf,
707 M., Schulze, E., Tomelleri, E., Ceschia, E., Bernhofer, C., Béziat, P., Carrara, A., Di Tommasi, P.,
708 Grunwald, T., Jones, M., Magliulo, V., Moureaux, C., Olioso, A., Sanz, M., Saunders, M., Søgaard, H.,
709 Ziegler, W.: The net biome production of full crop rotations in Europe, Agric. Ecosyst. Environ., 139(3),
710 336–345, https://doi.org/10.1016/j.agee.2010.07.016, 2010.
711 Kool, D., Agam, N., Lazarovitch, N., Heitman, J.L., Sauer, T.J., Ben-Gal, A.: A review of approaches for
712 evapotranspiration partitioning, Agric. For. Meteorol., 184, 56–70,
713 https://doi.org/10.1016/j.agrformet.2013.09.003, 2014.
714 Koster, R. D., and Suarez, M. J.: The Influence of Land Surface Moisture Retention on Precipitation Statistics.

J. Clim., 9(10), 2551–2567, https://doi.org/10.1175/1520-0442(1996)009, 1996.

Lawrence, D. M., Thornton, P. E., Oleson, K. W., and Bonan, G. B.: The Partitioning of Evapotranspiration into Transpiration, Soil Evaporation, and Canopy Evaporation in a GCM: Impacts on Land–Atmosphere Interaction, J. Hydrometeorol., 8, 862–880, https://doi.org/10.1175/JHM596.1, 2007.

Lehmann, P., Merlin, O., Gentine, P., and Or, D.: Soil texture effects on surface resistance to bare soil evaporation, Geophys. Res. Lett., 45(19), 10, 398-10, 405, https://doi.org/10.1029/2018GL078803, 2018.

Lemone, M. A., Chen, F., Alfieri, J. G., Cuenca, R. H., Hagimoto, Y., Blanken, P., Niyogi, D., Kang, S., Davis, K., Grossman, R. L.: NCAR/CU surface, soil, and vegetation observations during the International H2O Project 2002 field campaign, Bull. Am. Meteorol. Soc, 88(1), 65–81, https://doi.org/10.1175/BAMS-88-1-65, 2007.

Letts, M.G., Comer, N.T., Roulet, N.T., Skarupa, M.R., Verseghy, D.L.: Parametrization of peatland hydraulic properties for the Canadian land surface scheme, Atmos. Ocean., 38, 141–160, https://doi.org/10.1080/07055900.2000.9649643, 2000.

Leuning, R., Zhang, Y.Q., Rajaud, A., Cleugh, H., Tu, K.: A simple surface conductance model to estimate regional evaporation using MODIS leaf area index and the Penman–Monteith equation, Water Resour., Res. 44 (10), W10419, https://doi.org/10.1029/2007WR006562, 2008.

Liang, S., Cheng, J., Jia, K., Jiang, B., Liu, Q., Xiao, Z., Yao, Y., Yuan, W., Zhang, X., Zhao, X., Zhou, J.: The global land surface satellite (GLASS) product suite, Bull. Am. Meteorol. Soc., 102, E323–E337, https://doi.org/10.1175/BAMS-D-18-0341.1, 2021.

Liu, J., Chai, L., Dong, J., Zheng, D., Wigneron, J. P., Liu, S., Zhou, J., Xu, T., Yang, S., Song, Y., Qu, Y., Lu, Z.: Uncertainty analysis of eleven multisource soil moisture products in the third pole environment based on the three-corned hat method, Remote Sens. Environ., 255, 112225, https://doi.org/10.1016/j.rse.2020.112225, 2021.

Liu, S., Lu, L., Mao, D., and Jia, L.: Evaluating parameterizations of aerodynamic resistance to heat transfer using field measurements, Hydrol. Earth Syst. Sci., 11, 769–783, https://doi.org/10.5194/hess-11-769-2007, 2007.

Liu, S.M., Li, X., Xu, Z.W., Che, T., Xiao, Q., Ma, M.G., Liu, Q.H., Jin, R., Guo, J.W., Wang, L.X., Wang, W.Z., Qi, Y., Li, H.Y., Xu, T.R., Ran, Y.H., Hu, X.L., Shi, S.J., Zhu, Z.L., Tan, J.L., Zhang, Y., Ren, Z.G.: The Heihe Integrated Observatory Network: A Basin-Scale Land Surface Processes Observatory in China, Vadose Zo. J., 17(1), 180072, https://doi.org/10.2136/vzj2018.04.0072, 2018.

745 Liu, S. M., Xu, Z. W., Wang, W. Z., Jia, Z. Z., Zhu, M. J., Bai, J., and Wang, J. M.: A comparison of eddy-
746 covariance and large aperture scintillometer measurements with respect to the energy balance closure
747 problem, Hydrol. Earth Syst. Sci., 15, 1291–1306, https://doi.org/10.5194/hess-15-1291-2011, 2011.
748 Li, S., Hao, X., Du, T., Tong, L., Zhang, J., Kang, S.: A coupled surface resistance model to estimate crop
749 evapotranspiration in arid region of northwest China, Hydrol. Process., 28(4), 2312–2323,
750 https://doi.org/10.2136/vzj2018.04.0072, 2013.
751 Li, S., Wang, G., Sun, S., Chen, H., Bai, P., Zhou, S., Huang, Y., Wang, J., Deng, P.: Assessment of Multi-
752 Source Evapotranspiration Products over China Using Eddy Covariance Observations, Remote Sens.,
753 10(11), 1692, https://doi.org/10.3390/rs10111692, 2018.
754 Li, X., Liang, S., Yuan, W., Yu, G., Cheng, X., Chen, Y., Zhao, T., Feng, J., Ma, Z., Ma, M., Liu, S., Chen, J.,
755 Shao, C., Li, S., Zhang, X., Zhang, Z., Sun, G., Chen, S., Ohta, T., Varlagin, A., Miyata, A., Takagi, K.,
756 Saiqusa, N., Kato, T.: Estimation of evapotranspiration over the terrestrial ecosystems in China,
757 Ecohydrology, 7(1), 139–149, https://doi.org/10.1002/eco.1341, 2014a.
758 Li, X., Wang, L., Chen, D., Yang, K., and Wang, A.: Seasonal evapotranspiration changes (1983-2006) of four
759 large basins on the Tibetan Plateau, J. Geophys. Res. Atmos., 119(23), 13,079–13,095,
760 https://doi.org/10.1002/2014JD022380, 2014b.
761 Li, S., Zhang, L., Kang, S., Tong, L., Du, T., Hao, X., and Zhao, P.: Comparison of several surface resistance
762 models for estimating crop evapotranspiration over the entire growing season in arid regions, Agric. For.
763 Meteorol., 208, 1–15, https://doi.org/10.1016/j.agrformet.2015.04.002, 2015.
764 Ma, N., Szilagyi, J., Zhang, Y., Liu, W.: Complementary-Relationship-Based Modeling of Terrestrial
765 Evapotranspiration Across China During 1982–2012: Validations and Spatiotemporal Analyses, J.
766 Geophys. Res. Atmos., 124(8), 4326–4351, https://doi.org/10.1029/2018JD029850, 2019.
767 Ma, N., Zhang, Y.: Increasing Tibetan Plateau terrestrial evapotranspiration primarily driven by precipitation,
768 Agric. For. Meteorol., 317, 108887, https://doi.org/10.1016/j.agrformet.2022.108887, 2022.
769 Ma, N., Zhang, Y., Guo, Y., Gao, H., Zhang, H., Wang, Y.: Environmental and biophysical controls on the
770 evapotranspiration over the highest alpine steppe, J. Hydrol., 529, 980–992,
771 https://doi.org/10.1016/j.jhydrol.2015.09.013, 2015a.
772 Ma, N., Y. Zhang, C.-Y. Xu, and J. Szilagyi: Modeling actual evapotranspiration with routine meteorological
773 variables in the data-scarce region of the Tibetan Plateau: Comparisons and implications, J. Geophys. Res.
774 Biogeosci., 120, 1638–1657, https://doi.org/10.1002/2015JG003006, 2015b.

Ma, Y., Hu, Z., Xie, Z., Ma, W., Wang, B., Chen, X., Li, M., Zhong, L., Sun, F., Gu, L., Han, C., Zhang, L., Liu, X., Ding, Z., Sun, G., Wang, S., Wang, Y., and Wang, Z.: A long-term (2005–2016) dataset of hourly integrated land–atmosphere interaction observations on the Tibetan Plateau, Earth Syst. Sci. Data., 12, 2937–2957, https://doi.org/10.5194/essd-12-2937-2020, 2020.

Merlin, O., Stefan, V. G., Amazirh, A., Chanzy, A., Ceschia, E., Er-Raki, S., Khabba, S.: Modeling soil evaporation efficiency in a range of soil and atmospheric conditions using a meta-analysis approach, Water Resour. Res., 52(5), 3663–3684, https://doi.org/10.1002/2015WR018233, 2016.

Miralles, D. G., Holmes, T. R. H., De Jeu, R. A. M., Gash, J. H., Meesters, A. G. C. A., Dolman, A. J.: Global land-surface evaporation estimated from satellite-based observations, Hydrol. Earth Syst. Sci., 15(2), 453–469, https://doi.org/10.5194/hess-15-453-2011, 2011.

Miralles, D. G., Jiménez, C., Jung, M., Michel, D., Ershadi, A., McCabe, M. F., Hirschi, M., Martens, B., Dolman, A. J., Fisher, J. B., Mu, Q., Seneviratne, S. I., Wood, E. F., and Fernández-Prieto, D.: The WACMOS-ET project – Part 2: Evaluation of global terrestrial evaporation data sets, Hydrol. Earth Syst. Sci., 20, 823–842, https://doi.org/10.5194/hess-20-823-2016, 2016.

Muñoz-Sabater, J., Dutra, E., Agustí-Panareda, A., Albergel, C., Arduini, G., Balsamo, G., Boussetta, S., Choulga, M., Harrigan, S., Hersbach, H., Martens, B., Miralles, D., Piles, M., Rodríguez-Fernández, N., Zsoter, E., Thépaut, J. N.: ERA5-Land: A state-of-the-art global reanalysis dataset for land applications, Earth Syst. Sci. Data, 13(9), 4349–4383, https://doi.org/10.5194/essd-13-4349-2021, 2021.

Novick, K. A., Stoy, P. C., Katul, G. G., Ellsworth, D. S., Siqueira, M. B. S., Juang, J., Oren, R.: Carbon dioxide and water vapor exchange in a warm temperate grassland, Oecologia., 138(2), 259–274, https://doi.org/10.1007/s00442-003-1388-z, 2004.

Ortega-Farias, S., Poblete-Echeverría, C., and Brisson, N.: Parameterization of a two-layer model for estimating vineyard evapotranspiration using meteorological measurements, Agric. For. Meteorol., 150(2), 276–286, https://doi.org/10.1016/j.agrformet.2009.11.012, 2010.

Peng, J., Loew, A., Chen, X., Ma, Y., and Su, Z.: Comparison of satellite-based evapotranspiration estimates over the Tibetan Plateau. Hydrol, Earth Syst. Sci., 20, 3167–3182, https://doi.org/10.5194/hess-20-3167-2016, 2016.

Phillips, T. J., Klein, S. A., Ma, H. Y., Tang, Q., Xie, S., Williams, I. N., Joseph, A., David, R., Margaret, S.: Using ARM observations to evaluate climate model simulations of land-atmosphere coupling on the U.S. Southern Great Plains, J. Geophys. Res. Atmos., 122(21), 11,524–11, 548,

https://doi.org/10.1002/2017JD027141, 2017.

Ramoelo, A., Majozi, N., Mathieu, R., Jovanovic, N., Nickless, A., and Dzikiti, S.: Validation of Global Evapotranspiration Product (MOD16) using Flux Tower Data in the African Savanna, South Africa, Remote Sens.-Basel, 6, 7406–7423, https://doi.org/10.3390/rs6087406, 2014.

Rodell, M., Houser, P. R., Jambor, U., Gottschalck, J., Mitchell, K., Meng, C. J., Arsenault, K., Cosgrovem B., Radakovich, J., Bosilovich, M., Entin, J., Walker, J., Lohmann, D., Toll, D.: The Global Land Data Assimilation System, Bull. Am. Meteorol. Soc., 85, 381–394, https://doi.org/10.1175/BAMS-85-3-381, 2004.

Sakaguchi, K., Zeng, X.: Effects of soil wetness, plant litter, and under-canopy atmospheric stability on ground evaporation in the Community Land Model (CLM3.5), J. Geophys. Res., Atmos. 114(D1), https://doi.org/10.1029/2008JD010834, 2009.

Sellers, P. J., Randall, D. A., Collatz, G. J., Berry, J. A., Field, C. B., Dazlich, D. A., and Bounoua, L.: A Revised Land Surface Parameterization (SiB2) for Atmospheric GCMS. Part I: Model Formulation, J. Clim. 9(4), 676–705, https://doi.org/10.1175/1520-0442(1996)009<0676:ARLSPF>2.0.CO;2, 1996.

Shi, Q., Liang, S.: Surface-sensible and latent heat fluxes over the Tibetan Plateau from ground measurements, reanalysis, and satellite data, Amos. Chem. Phys.,14, 5659–5677, https://doi.org/10.5194/acp-14-5659-2014, 2014.

Sobrino, J. A., Jiménez-Muñoz, J. C., and Paolini, L.: Land surface temperature retrieval from LANDSAT TM 5, Remote Sens. Environ., 90(4), 434–440, https://doi.org/10.1016/j.rse.2004.02.003, 2004.

Song, L., Zhuang, Q., Yin, Y., Zhu, X., and Wu, S.: Spatio-temporal dynamics of evapotranspiration on the Tibetan Plateau from 2000 to 2010, Environ. Res. Lett., 12(1), 014011, https://doi.org/10.1088/1748-9326/aa527d, 2017.

Su, Z.: The Surface Energy Balance System (SEBS) for estimation of turbulent heat fluxes, Hydrol. Earth Syst. Sci., 6, 85–100, https://doi.org/10.5194/hess-6-85-2002, 2002.

Sun, S.F.: Moisture and heat transport in a soil layer forced by atmospheric conditions, Master thesis, Dept. of Civil Engineering, University of Connecticut, 72, 1982.

Tang, J. Y. and Riley, W. J.: A new top boundary condition for modeling surface diffusive exchange of a generic volatile tracer: theoretical analysis and application to soil evaporation, Hydrol. Earth Syst. Sci., 17, 873–893, https://doi.org/10.5194/hess-17-873-2013, 2013.

Wang, B., Ma, Y., Su, Z., Wang, Y., and Ma, W.: Quantifying the evaporation amounts of 75 high-elevation

large dimictic lakes on the Tibetan Plateau, Sci. Adv., 6(26), https://doi.org/10.1126/sciadv.aay8558, 2020.

Wang, G., Lin, S., Hu, Z., Lu, Y., Sun, X., and Huang, K.: Improving Actual Evapotranspiration Estimation Integrating Energy Consumption for Ice Phase Change Across the Tibetan Plateau, J. Geophys. Res. Atmos., 125(3), e2019JD031799, https://doi.org/10.1029/2019JD031799, 2020.

Wang, W., Li, J., Yu, Z., Ding, Y., Xing, W., Lu, W.: Satellite retrieval of actual evapotranspiration in the Tibetan Plateau: components partitioning, multi decadal trends and dominated factors identifying, J. Hydrol., 559, 471–485, https://doi.org/10.1016/j.jhydrol.2018.02.065, 2018.

Wang, Y., Lv, W., Xue, K. et al. Grassland changes and adaptive management on the Qinghai–Tibetan Plateau. Nat. Rev. Earth. Environ 3, 668–683 (2022). https://doi.org/10.1038/s43017-022-00330-8

Wieder, W.R., J. Boehnert, G.B. Bonan, and M. Langseth.: Regridded Harmonized World Soil Database v1.2. Data set, Available on-line [http://daac.ornl.gov] from Oak Ridge National Laboratory Distributed Active Archive Center, Oak Ridge, Tennessee, USA, http://dx.doi.org/10.3334/ORNLDAAC/1247, 2014.

Wilcox, B.P., Breshears, D.D., Seyfried, M.S.: Water balance on rangelands, In: Stewart, B.A., Howell, T.A. (Eds.), Encyclopedia of Water Science, Marcel Dekker Inc, New York, 791–794, http://www.cprl.ars.usda.gov/wmru/pdfs/DekkerEvettTDR.pdf, 2003.

Wu, C., Hu, B. X., Huang, G., and Zhang, H.: Effects of climate and terrestrial storage on temporal variability of actual evapotranspiration, J. Hydrol., 549, 388–403, https://doi.org/10.1016/j.jhydrol.2017.04.012, 2017.

Yang, K., He, J., Tang, W., Qin, J., Cheng, C. C. K.: On downward shortwave and longwave radiations over high altitude regions: Observation and modeling in the Tibetan Plateau, Agric. For. Meteorol., 150(1), 38–46, https://doi.org/10.1016/j.agrformet.2009.08.004, 2010.

Yang, K., Koike, T., Ishikawa, H., Kim, J., Li, X., Liu, H., Liu S., Ma Y., Wang, J.: Turbulent flux transfer over bare-soil surfaces: Characteristics and parameterization, J. Appl. Meteorol. Climatol., 47(1), 276–290, https://doi.org/10.1175/2007JAMC1547.1, 2008.

Yang, K., Wu, H., Qin, J., Lin, C., Tang, W., and Chen, Y.: Recent climate changes over the Tibetan Plateau and their impacts on energy and water cycle: A review, Glob. Planet. Change., 112, 79–91, https://doi.org/10.1016/j.gloplacha.2013.12.001, 2014.

Yang, Y., Liu, Y., Li, M., Hu, Z., Ding, Z.: Assessment of reanalysis flux products based on eddy covariance observations over the Tibetan Plateau, Theor. Appl. Climatol., 138, 275–292, https://doi.org/10.1007/s00704-019-02811-1, 2019.

Yao, T., Thompson, L., Yang, W., Yu, W., Gao, Y., Guo, X., Yang, X., Duan, K., Zhao, H., Xu, B., Pu, J., Lu,

A., Xiang, Y., Kattel, D., Joswiak, D.: Different glacier status with atmospheric circulations in Tibetan Plateau and surroundings, Nature Clim.Change, 2(9), 663–667, https://doi.org/10.1038/nclimate1580, 2012.

Yao, Y., Liang, S., Cheng, J., Liu, S., Fisher, J. B., Zhang, X., Jia, K., Zhao, X., Qin, Q., Zhao, B., Han, S., Zhou, G., Li, Y., Zhao, S.: MODIS-driven estimation of terrestrial latent heat flux in China based on a modified Priestley-Taylor algorithm, Agric. For. Meteorol., 171–172, 187–202, https://doi.org/10.1016/j.agrformet.2012.11.016, 2013.

Yin, Y., Wu, S., Zhao, D., Zheng, D., Pan, T.: Modeled effects of climate change on actual evapotranspiration in different eco-geographical regions in the Tibetan Plateau, J. Geogr. Sci., 23(2), 195–207, https://doi.org/10.1002/eco.1341, 2013.

You, Q., Xue, X., Peng, F., Dong, S., Gao, Y.: Surface water and heat exchange comparison between alpine meadow and bare land in a permafrost region of the Tibetan Plateau, Agric. For. Meteorol., 232, 48–65, https://doi.org/10.1016/j.agrformet.2016.08.004, 2017.

Yuan, L., Ma, Y., Chen, X., Wang, Y., Li, Z.: An enhanced MOD16 evapotranspiration model for the Tibetan Plateau during the unfrozen season, J. Geophys. Res. Atmos., 126, e2020JD032787, https://doi.org/10.1029/2020JD032787, 2021.

Yu, G. R., Wen, X. F., Sun, X. M., Tanner, B. D., Lee, X., Chen, J. Y.: Overview of ChinaFLUX and evaluation of its eddy covariance measurement, Agric. For. Meteorol., 137(3–4), 125–137, https://doi.org/10.1016/j.agrformet.2006.02.011, 2006.

Zhang, G., T. Yao, H. Xie, K. Yang, L. Zhu, C. K. Shum, T. Bolch, S. Yi, S. Allen, L. Jiang, W. Chen, and C. Ke: Response of Tibetan Plateau lakes to climate change: Trends, patterns, and mechanisms, Earth-Science Reviews, 103269. https://doi.org/10.1016/j.earscirev.2020.103269, 2020.

Zhang, L. M., Luo, Y. W., Liu, M., Chen, Z., Su, W., He et al.: Carbon and water fluxes observed by the Chinese Flux Observation and Research Network (2003–2005) (in Chinese), Sci. Data., 4(1), https://doi.org/10.11922/csdata.2018.0028.zh, 2019a.

Zhang, K., Kimball, J. S., Nemani, R. R., and Running, S. W.: A continuous satellite-derived global record of land surface evapotranspiration from 1983 to 2006, Water Resour. Res., 46(9), W09522, https://doi.org/10.1029/2009WR008800, 2010.

Zhang, Y., Kong, D., Gan, R., Chiew, F. H. S., McVicar, T. R., Zhang, Q., and Yang, Y.: Coupled estimation of 500 m and 8-day resolution global evapotranspiration and gross primary production in 2002–2017,

Remote Sens. 820 Environ., 222, 165–182, https://doi.org/10.1016/j.rse.2018.12.031, 2019b.

Zhang, Y., Peña-Arancibia, J. L., McVicar, T. R., Chiew, F. H. S., Vaze, J., Liu, C., Lu, X., Zheng, H., Wang, Y., Liu, Y., Miralles, D., Pan, M.: Multi-decadal trends in global terrestrial evapotranspiration and its components, Sci. Rep., 6, 19124, https://doi.org/10.1038/srep19124, 2016.

Zhao, H., Zeng, Y., Lv, S., and Su, Z.: Analysis of soil hydraulic and thermal properties for land surface modeling over the Tibetan Plateau, Earth Syst. Sci. Data., 10, 1031–1061, https://doi.org/10.5194/essd-10-1031-2018, 2018.

Zheng, D., Zhang, Q., Wu, S.: Mountain genecology and sustainable development of the Tibetan Plateau, Springer Science & Business Media, 57, 2000.

Zhong, L., Ma, Y., Hu, Z., Fu, Y., Hu, Y., Wang, X., Cheng, M., and Ge, N.: Estimation of hourly land surface heat fluxes over the Tibetan Plateau by the combined use of geostationary and polar-orbiting satellites, Atmos. Chem. Phys., 19, 5529–5541, https://doi.org/10.5194/acp-19-5529-2019, 2019.

Zohaib, M., H. Kim, and M. Choi.: Evaluating the patterns of spatiotemporal trends of root zone soil moisture in major climate regions in East Asia, J. Geophys. Res. Atmos., 122, 7705–7722, https://doi.org/10.1002/2016JD026379, 2017.